Stiffness Prediction Methods for Additively Manufactured Lattice Structures

by

Charlotte Méry Folinus

Submitted to the Department of Mechanical Engineering
in partial fulfillment of the requirements for the degree of

Bachelor of Science in Engineering
as Recommended by the Department of Mechanical Engineering

at the

MASSACHUSETTS INSTITUTE OF TECHNOLOGY

May 2020

Author ....
Department of Mechanical Engineering
May 8, 2020

Certified by..
Anette "Peko" Hosoi
Neil and Jane Pappalardo Professor of Mechanical Engineering
Associate Dean of Engineering
Thesis Supervisor

Accepted by ....
Maria Yang
Professor of Mechanical Engineering
Undergraduate Officer

Stiffness Prediction Methods for Additively Manufactured Lattice Structures

by

Charlotte Méry Folinus

Submitted to the Department of Mechanical Engineering
on May 8, 2020, in partial fulfillment of the
requirements for the degree of
Bachelor of Science in Engineering
as Recommended by the Department of Mechanical Engineering

Abstract

Since the initial 300 pair release of the Futurecraft 4D in April 2017, adidas has scaled its 4D program to mass produce additively manufactured shoe midsoles. The 4D midsoles are constructed from lattice structures, and if there is variation in the manufacturing process, the structure's material and/or geometric properties may be altered. This means midsoles may have the same geometry but different material properties and thus different stiffnesses, and they may also have the same material properties but different overall stiffness due to geometric changes. The current quality control test is slow, expensive, and does not scale well.

This thesis explores two potential techniques: using ultrasonic waves to determine the lattices' acoustic properties, and weighing them to determine their mass. Pulse-echo testing data for $n = 8$ samples shows a statistically significant ($p = 0.0398 < 0.05$) increase in response time due to sample stiffness. Stiffness scaled linearly with lattice mass for both physical and simulated lattices, and mass predicted lattice stiffness with a minimum accuracy of 90% across a range of simulated manufacturing conditions. An analytical framework parameterized around a bivariate normal distribution can determine accuracy of new test methods or from additional mass-stiffness data. Lastly, cost minimization is presented for a hybrid test protocol which combines mass testing with secondary testing for rejected samples. At specification limits of $\pm 1\sigma$, the hybrid test achieves 99% accuracy at 69.8% of the cost for the current test. Increasing the specification limit to $\pm 2\sigma$ reduces cost further, achieving 99% accuracy at 16.4% of the current cost.

Thesis Supervisor: Anette "Peko" Hosoi
Title: Neil and Jane Pappalardo Professor of Mechanical Engineering
Associate Dean of Engineering

Acknowledgments

This thesis, like much of what I have accomplished at MIT, would not have been possible without the unfailing support of many individuals and communities. Many people made MIT special and kept me smiling and laughing (for the most part) no matter what happened.

My advisors, Prof. Anette "Peko" Hosoi at MIT and Chris Polster at adidas, gave me an exciting project which challenged me to grow as an engineer and researcher. Their insightful questions encouraged curiosity, pushing me to think more deeply. Chris and his team at adidas have inspired me to apply engineering analysis to unique problem spaces. Chris helped me focus this research by thinking about its impact and future usefulness. I am also grateful to our partners at adidas for the opportunity to work for three months in Herzogenaurach.

I could write a separate thesis detailing the ways Peko's presence has improved my life, and I still would not come close to capturing her true impact. She has been a voice of reason while radiating excitement and positivity. To Peko, a prototype is not a failure, scatter is not worthless, and you are not a bad engineer as long as you are able to learn from the experience. When I stumbled along the way, she provided both thoughtful critique and encouragement to still believe my work. I am privileged to work with Peko, someone who epitomizes MIT's best values and represents much of who I strive to be as an engineer, collaborator, and person.

My labmates on Team Peko helped me appreciate both the excitement and navigate the uncertainties of research. Sarah Fay was an excellent guide, helping me build confidence and competence as a researcher and answering my many questions. I am happy she both convinced me to write this thesis.

I am in debt to the people who have taught me everything I know about mechanical design and fabrication. Geoff Tsai first ignited my passion for design in 2.007. The Pappalardo and LMP shop staff constantly supported me for the last three years — challenging me to grow and laughing with me the many times I failed. Joe Wight fostered my curiosity, built an excitement for manufacturing, and let me play with new tools. Dr. Daniel Braunstein and his relentless crew of Bill Cormier, Jim Dudley, Steve Haberek, Tasker Smith, and Scott Spence made a basement into a home. Danny was always ready to patiently listen and offer a calming perspective in a variety of design and life challenges. Danny taught me to celebrate learning and strive for greater balance in all things; his compassion and empathy inspire me to become a better engineer and person.

My godparents, Kate and Jerry, encouraged me to have fun with all I do. Kate's chocolate kept me well-fueled throughout my thesis-ing, and she reminds me to never take things too seriously. Jerry taught me stubborn persistence and the power of numbers. I like to think he would have enjoyed reading this. My parents, Marilyn and Jeffrey, taught me to strive for excellence and challenge myself. They showed me the value of hard work, pushed me to be my best, and encouraged me to chase my dreams. They always remind me to follow my heart, go on adventures, and trust that life will fall into place if I do what I love.

Thank you all for the countless opportunities to play, to learn, and to grow.

Contents

List of Figures

List of Tables

Chapter 1

Introduction

The goal of this thesis was to develop a test to predict the stiffness of additively manufactured lattice structures. This work was motivated by our partner, the adidas FUTURE team, based in Portland (Oregon, USA) and Herzogenaurach (Germany). adidas currently uses additive manufacturing to produce running shoes. An accurate, fast, and low cost inspection technique could be further developed and applied as a manufacturing quality control test.

adidas is the largest sportwear manufacturer in Europe and the second-largest globally behind Nike (Beaverton, Oregon, USA) [64]. Valued at 61 billion USD globally in 2018 [45], the athletic footwear market constitutes a large portion of sneaker sales, which reached 100 billion USD in 2019 [66]. The sneaker industry grew significantly in recent years; sales have nearly doubled since 2016 [66]. Comprising both men's and women's sales, the athletic footwear category is projected to see continued growth at a rate of 7.9% per year for a total of 90 billion USD in global sales by 2023 [45].

Athletic footwear has historically been designed around average users, largely based off of white male anthropometry. This approach neglects users outside of existing standards, including those with different gender or ethnic backgrounds. Female runners now begin to outnumber men in many running events and organizations, increasing the demand for female-specific products. Advances in manufacturing technology can facilitate more inclusive designs by creating products tailored or customized for individual users.

Additive manufacturing (AM), also known as 3D printing, is a potential option for creating custom running shoes. Due to its high design flexibility and independence from costly mold tooling, shoes could be quickly adjusted and optimized for specific runners. AM is by no means a fundamentally new manufacturing process; the theory emerged in the 1970's [39], and practical origins trace their routes to the 1980's [36, 46]. However, footwear is a novel application of AM technology. Adapting any process for a new area produces significant variability as individual steps are refined and the process becomes better controlled. Quality control of AM footwear is necessary to ensure it meets required specifications, and these inspection techniques must be able to scale with production numbers. This thesis focuses on developing test methods which can predict the stiffness of a lattice without using a compression test.

Running shoe construction is described in Section 1.1. Section 1.2 gives an overview of AM methods and identifies several sources of variability in lattice manufacturing. Section 1.3 provides context on existing running shoe testing, which ranges from initial concept development to monitoring manufacturing processes. Preliminary work on this topic began through a class project in Spring 2019, which is discussed in Section 1.4. Finally, an overview of the thesis is outlined in Section 1.5.

1.1 Running Shoe Midsoles

Running shoes aim to prevent injury, give traction with the running surface, and optimize a runner's performance. While running shoes may have additional subcomponents or detailing, the major components are the upper, midsole, and outsole, as shown in Figure 1-1. The upper wraps around the top and sides of the foot and holds the shoe to the foot [26]. The upper often contains a heel counter, a stiff insert which secures the foot by guiding the heel and preventing excessive motion. The midsole is the primary source of cushioning, traditionally made of polymer foam. The outsole provides traction and protects the midsole [16]. The insole sits below the foot, separating it from the seams and adhesives which secure the upper and midsole. While some work has focused on insoles or other forms of shoe inserts [47, 49], the midsole is often the focus of research and development [48, 54, 56, 68, 33, 67]. Of these components, the midsole is most closely associated with runner performance, which is often seen as a minimization of lost energy [50] or running economy [33]. Previous work associates midsole bending stiffness with decreased energy losses, enhanced aerobic capability, and improved performance [54, 33].

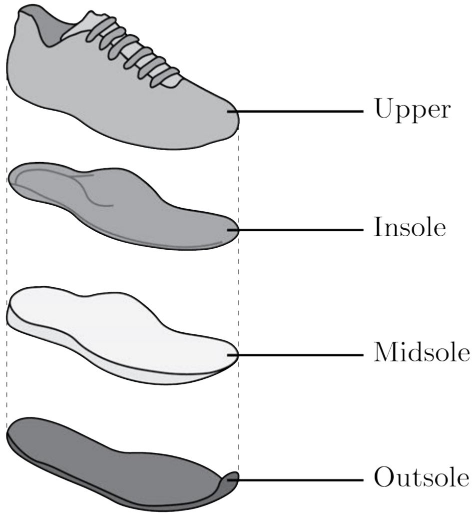

Figure 1-1: Exploded view of a running shoe, displaying its major components. Adapted from [51].

Running shoe midsoles are traditionally produced in molding processes from closed cell foams. These viscoelastic foams, traditionally ethyl vinyl acetate (EVA, Figure 1-2a) or polyurethane (PU) [67], offer good damping and heat dissipation properties [41]. In recent years, companies have introduced new polymers and foams: Nike's Vaporfly shoe (Figure 1-2b) uses polyether block amide (PEBA) foam, marketed as PEBAX (Arkema, Colombes, France) and VESTAMID E (Evonik Industries, Essen, Germany) [55]; and adidas's Boost (Figure 1-2c) creates a foam from expanded thermoplastic polyurethane (eTPU) particles [2]. Both PEBA and eTPU offer improved energy return properties compared to industry standards such as EVA. Despite this performance benefit, both PEBA and eTPU are constrained by mold-based manufacturing processes which prevent easy modification of midsoles for individual users.

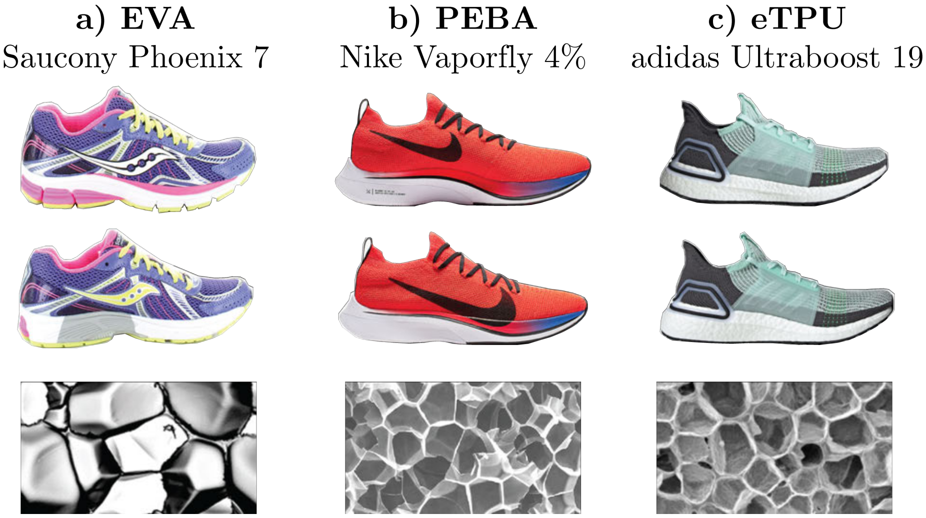

a) EVA
Saucony Phoenix 7

b) PEBA
Nike Vaporfly 4%

c) eTPU
adidas Ultraboost 19

Figure 1-2: Traditional running shoe midsoles are manufactured using closed-cell foams such EVA, PEBA, and eTPU [58], [52], and [4].

Achieving different foam densities or variable stiffness regions using traditional manufacturing methods requires gluing several foams together. In 1993, Saucony's Hello EVA combined different foams to create the first dual-density midsole, offering improved cushioning and stability [37]. This set a new industry standard for shoe performance. Today, shoes like the Saucony Phoenix 7 in Figure 1-2 use higher density inserts to provide stability and reduce pronation, the inward movement of the foot during running. Companies also developed other ways to improve midsoles; a few advances are displayed in Figure 1-3. Despite experiments with adding leaf springs [32] and air cushions [63], foam midsoles remain the industry standard.

1.1.1 adidas Futurecraft 4D

Several companies are developing AM midsoles as an alternative to foam midsoles [62]. adidas creates elastomeric lattice structures using a proprietary process from Carbon 3D (Redwood City, California, USA). The adidas Futurecraft 4D program launched in April 2017 with the initial 300 pair release of the Futurecraft 4D shoe, shown in Figure 1-3c [61]. Midsoles are created from a digital geometry, which pro-

a) Leaf springs
adidas Springblade

b) Air cushions
Nike Air Max

c) Lattice structures
adidas AlphaEdge

Figure 1-3: Novel running shoe midsole technologies include a) leaf springs [59], b) air cushions [53], and c) elastomeric lattices [21].

vides increased design flexibility; midsoles can be customized by digitally adjusting the lattice structure. By translating athlete data into midsole stiffness profiles, each midsole can be designed for specific energy return, cushioning, and stability properties. adidas produces these midsoles at scale; the company produced more 100,000 pairs of shoes by the end of 2018 and continues to scale its process [3].

1.2 Additive Manufacturing

In contrast to other manufacturing methods, additive manufacturing creates parts by sequentially depositing material. Formative manufacturing, represented in Figure 1-4a, fills a mold cavity with material to create the desired geometries. Formative methods include processes such as injection molding, casting, and steam-chest molding of foams. Traditional foam midsoles are made using formative processes. Fabricating the necessary molds for these processes is costly, and parts are limited to geometries which can be easily filled and released from molds. Subtractive manufacturing removes material through methods such as machining (Figure 1-4b), electrical discharge machining (EDM), and laser cutting. Compared to formative techniques, subtractive manufacturing methods have increased design flexibility, but this comes at increased cost and reduced production speed.

Traditional additive manufacturing creates parts by building individual layers that bond to each other. The most mainstream techniques include fused deposition modeling (FDM/FFF, such as in Figure 1-4c and 1-5), stereolithography (SLA) as in Figure 1-6, multijet modeling (MJM), and selective laser sintering (SLS). Although these methods differ in how they make individual layers, each performs a series of discrete steps for every layer. Carbon's Digital Light Synthesis (DLS) and Continuous

Liquid Interface Process (CLIP) fundamentally differ from other techniques. Instead of performing a set of steps for individual layers, it continuously produces material and parts, leading to increased manufacturing speed.

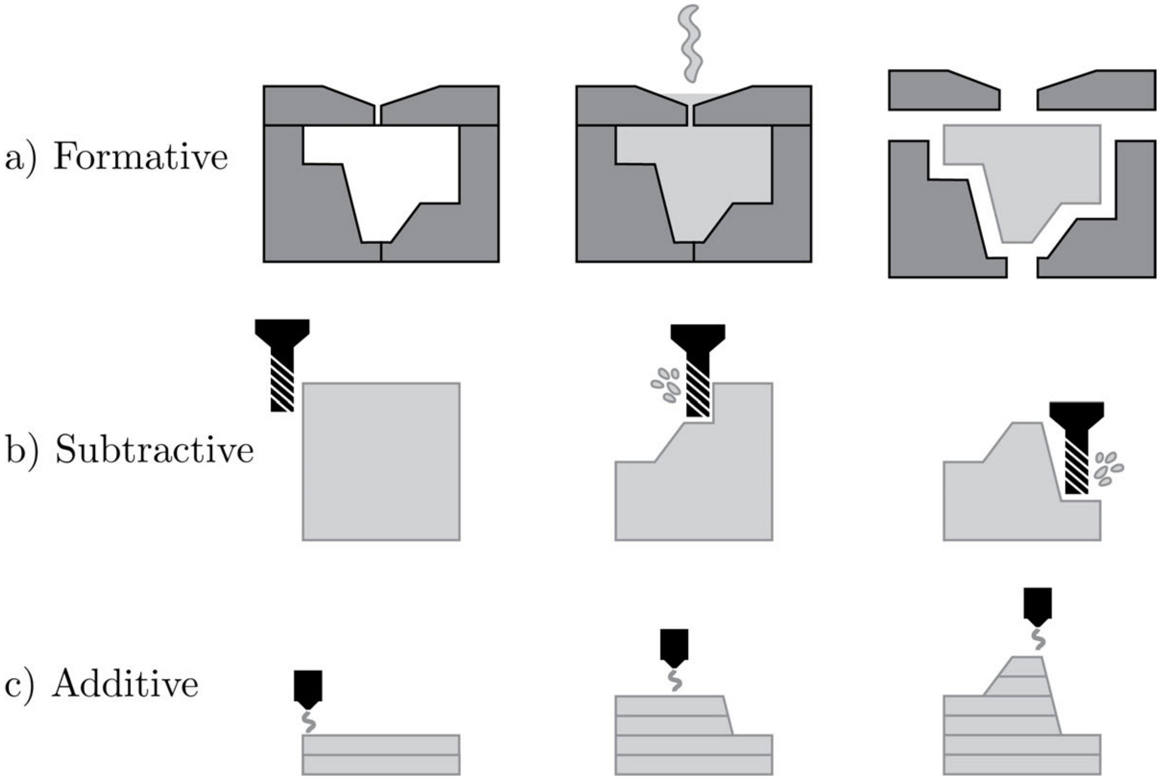

Figure 1-4: Schematic of the fundamental differences between formative, subtractive, and additive manufacturing methods. Adapted from [10] .

1.2.1 Layer-Based Processes

In fused deposition modeling (FDM), also referred to as fused filament fabrication (FFF), the machine heats a thermoplastic filament and extrudes it through the nozzle, a small opening in an extrusion die [40]. Figure 1-5 depicts this process. Software controls the position of the extruder relative to the printed part. A Cartesian robot typically moves the extruder along a two-dimensional path within each layer. After completing each layer, the table height adjusts to move the extruder to the next layer. FDM machines generate overhangs by printing a support structure. These support structures are printed using structures and/or material that is easily removable. Some machines produce support material with a less stiff filling structure that can be easily broken off of the finished part, while others use materials that dissolve in specialized solutions. Layer height is limited by the diameter of the opening in the extrusion die but typically ranges from 0.050 to 0.120 mm. For the same two-dimensional path, printing time is relatively similar regardless of layer height; as a result, print time is driven by the number of layers. FDM's layer-wise creation of parts results in stepped surfaces and anisotropic properties. FDM parts are stiff in tension and compression, but layers shear past each other relatively easily.

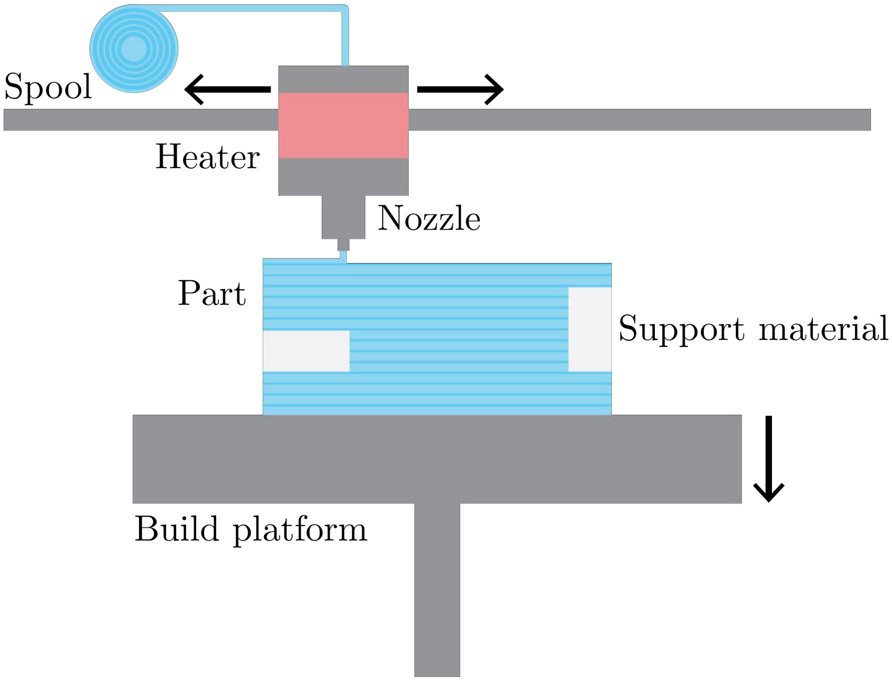

Figure 1-5: Schematic of the fused deposition modeling (FDM) process

Stereolithography (SLA) involves selectively curing a liquid photopolymer to create a solid object. This technique has been popularized by Formlabs (Somerville, Massachusetts, USA), which uses an upside-down SLA process in its machines, as represented in Figure 1-6. An ultraviolet laser focuses on a selected area within a shallow layer of the liquid polymer within a much larger resin tank. Galvanometers, small and precise motors, adjust the laser's position to move it around the XY plane and cure the photopolymer within a single layer of the part [25].

Part tolerance and resolution is driven by the laser's focus and sharpness but is typically as small as 0.0125 mm. SLA machines create stiff lattice structures to support parts and overhanging features during production. After curing a single layer, a series of mechanical steps occur to move the build platform, renew the resin, and cover the cured solid with a new layer of liquid polymer. Printing and curing time for each layer is similar regardless of thickness, but these discrete, mechanical steps must happen for each layer. As a result, SLA is rate-limited by the time required to perform the intermediate steps. After printing, support structures are mechanically removed from thee part, typically leaving blemish marks. SLA parts must also undergo washing to dissolve uncured material and UV curing to ensure a complete cure.

In multijet modeling (MJM), print heads deposit photopolymer on a build tray. Because UV bulbs cure each layer and cause it to harden into a solid, multijet modeling does not require post-print curing, unlike SLA printing. In addition to the

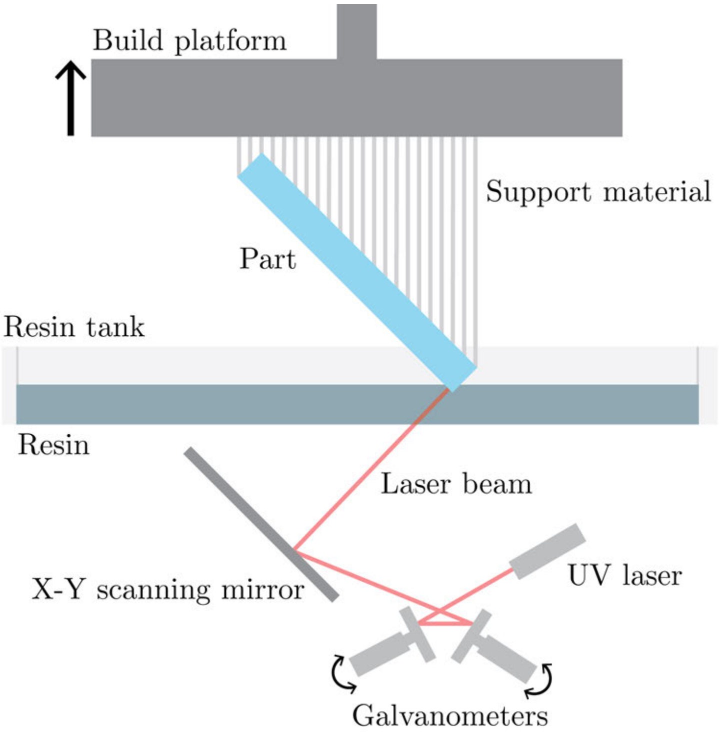

Figure 1-6: Schematic of the upside-down stereolithography (SLA) process used by Formlabs. Adapted from [25].

material used for the desired part, multijet machines also deposit a gel-like resin which acts as a support material and dissolves in an aqueous solution after printing. Like SLA, MJM also produces small surface layers. These layers are often as small as 0.016 mm, and the process is rate-limited by the time necessary to individually cure each layer.

Selective laser sintering (SLS) sinters nonmetallic powders into a solid object. When metallic powders are used, the process is referred to as selective metal melting (SLM). In SLS/SLM, a laser beam traces a particular cross section in a thin layer of powder. This sinters the powder particles into a solid mass. After covering this solidified layer with a new layer of powder, the process repeats for the next layer.

1.2.2 Digital Light Synthesis

Digital Light Synthesis, Carbon 3D's proprietary manufacturing technique, uses Continuous Liquid Interface Process (CLIP) to create monolithic parts with high resolution, good surface finish, and isotropic properties. This technique is used in Carbon's printers (Figure 1-7) to mass-produce parts in a variety of fields from sports equipment (Figures 1-3c and 1-8a-b) to dental devices (Figure 1-8c).

CLIP conducts stereolithography above an oxygen-permeable window, as shown in Figure 1-9 and detaild in [65, 38]. This window, made of an amorphous fluoropolymer (Teflon AF 2400) is chemically inert, transparent to UV waves, and oxygen-permeable. This creates a dead zone of uncured, liquid resin between the window and the part.

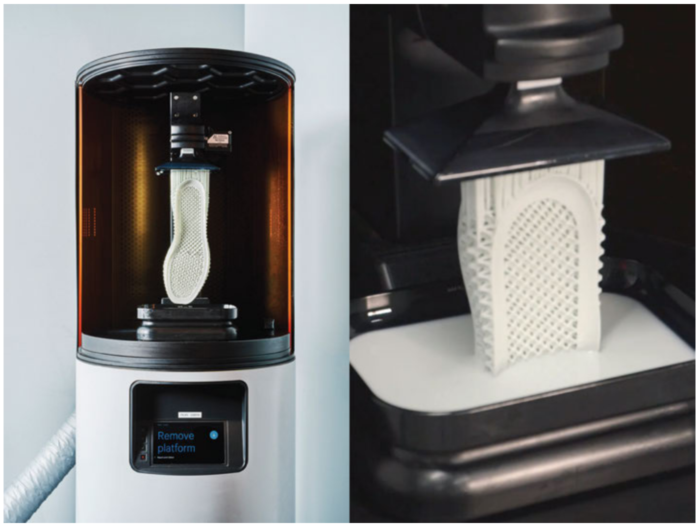

Figure 1-7: Carbon's M-series printers manufacture Futurecraft 4D midsoles in production [23] .


a) Specialized saddle b) Riddell helmet c) Dentsply dentures

Figure 1-8: Example applications of Carbon's AM technology in a variety of fields from athletic equipment to medical/dental devices [13, 14, 12].

The dead zone inhibits photopolymerization, meaning that resin will only cure due to selective UV light exposure. A continuous sequence of UV images is projected through the oxygen-permeable window, curing the resin. As the UV images cure the resin, the build platform lifts, continuously pulling the finished part out of the resin tank.

Unlike traditional stereolithography, where UV exposure, resin renewal, and part movement occur in separate steps, these occur continuously in CLIP. Although layer height and resolution affect printing rate in stereolithography, these factors do not impact production rate in CLIP. CLIP is instead rate-limited by the resin's material properties, particularly its cure rate and viscosity. As a result, CLIP produces parts at rates up to 100 times faster than other AM techniques.

Carbon focuses on printing metamaterials, specifically lattice structures. Additive manufacturing does not require producing complex tooling, which means parts, and specific regions of the parts, can be tailored for specific customer or functional needs. Carbon's software combines lattice parameters with material properties and desired mechanical behavior to generate metamaterials. Lattices can be tuned to achieve spe-

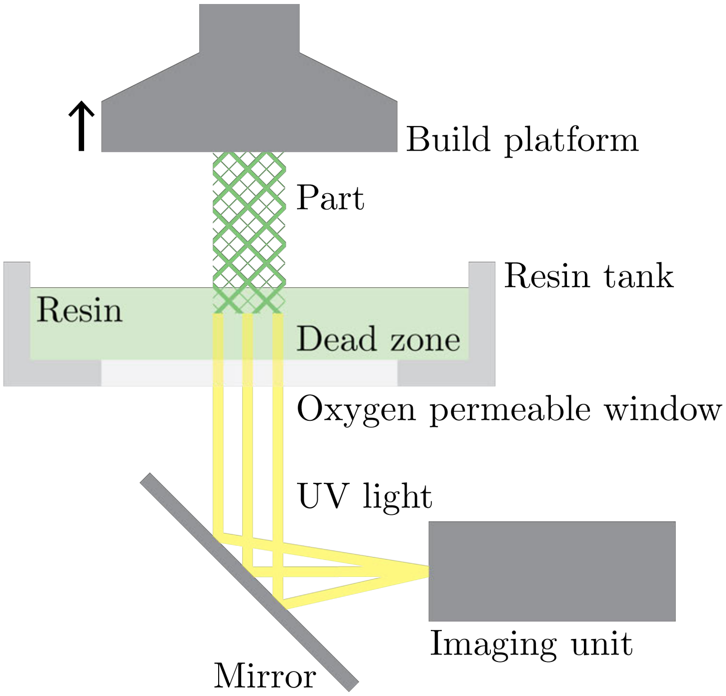

Figure 1-9: Schematic of the digital light synthesis process used by Carbon. Adapted from [65].

cific loading behaviors, including non-linear compression responses. Structures may also have multiple functional zones with different properties. Protective equipment typically uses expanded polystyrene to absorb impact, but optimizing performance means costly assembly of various parts. Riddell manipulates lattice geometry to create single-part football liners from a highly damped elastomer, shown in Figure 1-8b.

1.3 Shoe Quality Testing

Running shoes undergo rigorous testing at all stages of development, from initial concept to final product ready for release. Before a new product can be introduced to markets, many aspects of the product and the production line which creates it must be tested. In a shoe, individual materials such as the upper's textiles or the midsole's foam might be tested to establish material properties or understand fatigue behavior. As a shoe moves toward release, testing may become higher level, focusing on whole-shoe behavior, insurance of quality standards, or variability in the manufacturing line.

1.3.1 Research and Development

In the earliest stages of a new footwear product concept, experimental work emphasizes science such as materials fundamental biomechanics and materials science.

Motion capture and VO2 max testing help scientists understand how different shoe concepts affect running. In motion capture testing, a subject wears reflective markers on key anatomical locations, such as the sides of the ankle. An array of specialized cameras track marker position in three dimensions and create a digital representation of the runner's position in space. In addition to kinematic markers, force plates and EMG sensors often record ground reaction forces and muscle activity, respectively.

Among other metrics, joint powers and muscle activity may be used to compare shoes [68]. VO2 max testing uses a face mask to measure the volume and concentrations of inhaled and exhaled air during activity. VO2 max represents the maximal rate of oxygen consumption, which is typically seen as a good indicator of cardiovascular fitness. In addition to establishing the VO2 max, this type of testing is also used to determine running economy, defined as the rate of oxygen intake at a specified running speed. Running economy is linked to shoe performance: if a runner is more efficient in a given shoe, they might reasonably sustain faster speeds and improved performance [33].

At this stage, mechanical testing may focus on testing individual materials or performance of early prototypes. This could include compression or tensile testing in quasi-static and/or dynamic loading conditions. Fatigue behavior and properties in variable temperature conditions may also be important. As shoes progress in development, testing may also involve computational models of the product's properties or the manufacturing processes used to create it [17]. For example, development of the adidas Springblade, shown in Figure 1-3, included finite element simulations to determine the proper behavior of individual leaf springs [30, 31].

1.3.2 Quality Standards

Athletic companies test product quality against a variety of test standards, which any product must pass before it may be released. While some of these are internal quality requirements, others are developed according to International Standard Organization's (ISO) guidelines. Many quality standards focus on behavior in mechanical lifecycle testing. Among other standards, shoes must satisfy requirements for midsole compression, four point bending, and Martindale abrasion tests. Running shoes must also undergo an extended wear test of 400 km, typically lasting 8 weeks.

1.3.3 Inline Manufacturing Testing

Traditional manufacturing methods such as injection or steam-chest molding involve filling a mold with the midsole material. Due to fixed mold geometries, manufacturing variability mainly originates from differences in material properties, such as its density. As a result, simple measurements such as mass quickly capture the quality of standard foam midsoles.

The large number of production settings and steps, coupled with machine variability, mean that AM midsoles may not match the desired stiffness. In the existing production line, a midsole is inspected after the final post-processing step. The midsole is secured and undergoes a quasi-static compression test using a proprietary test fixture and test sequence.

This quasi-static test compresses midsoles a prescribed amount and uses the force readout to determine midsole viability. Midsoles meeting desired stiffness requirements proceed to later steps in the assembly process. Midsoles which do not meet these standards are rejected. As adidas and Carbon refine the printing process, the variability in produced parts is expected to decrease. In order to produce more pairs of shoes with consistent stiffnesses, adidas would then narrow the band of acceptable stiffnesses.

Unfortunately, a compression test does not scale well, and replacement test methods must capture both geometric and material variation within the lattice in order to be viable.

1.4 Preliminary Work through 2.98/2.980

Initial work on this topic began in Sports Technology: Engineering & Innovation, a course taught by Prof. Anette "Peko" Hosoi and lecturer Christina Chase at the Massachusetts Institute of Technology in Spring 2019 under course number 2.98/2.980. In 2.98/2.980, students attend lectures and work in small groups on industry projects. Lectures focus on technical strategies, trends in the sports technology field, and data analysis and representation. Industry leaders also give guest lectures highlighting their work. Partner companies and organizations sponsor projects on a range of topics, from analyzing player tracking data in soccer to quantifying team strategies in e-sports and studying vision through ski goggle lenses. Partners work with the course instructors to create project statements, outline student deliverables, and identify potential resources in the MIT community.

adidas presented the same problem statement to the Spring 2019 class which formed the basis of this work [34]. Over the course of the semester, the group brainstormed possible solutions, obtained compression testing data for sample lattices, and created bench level tests for four potential test methods: inducing lattice vibrations, image analysis to determine strut thickness, a ball drop test, and ultrasonic wave propagation. Given the damping properties of the lattice samples, the group struggled to produce large vibrations and accurately measure the deflection of the samples.The image analysis algorithm and setup were not robust enough to capture and analyze the lattice structure, but a more refined setup and complex machine learning algorithm could potentially better predict lattice stiffness due to variations in its geometry. Releasing a metal ball over the sample and measuring its rebound height did not yield repeatable results and showed no correlation with sample stiffness. Ultrasonic wave propagation was the most promising, but an under constrained test setup resulted in high uncertainty and low repeatability [15].

1.5 Thesis Outline

This thesis describes the work that led to the creation of a preliminary test method for evaluating the stiffness lattice-based midsoles. It is primarily focused on determining stiffness of lattice samples through compression, ultrasonic wave propagation, and mass testing.

Chapter 2: Mechanical Behavior of Physical Lattices: This chapter introduces the lattices used for this study, analyzes their predicted behavior, and discusses their observed properties such as mass, volume, and density.

Chapter 3: Acoustic Properties of Lattice Structures: The background of ultrasonic testing and the method utilizing it are introduced. Both the apparatus and experiment designs are discussed, and results are presented correlating test performance with the known stiffness values established in Chapter 2.

Chapter 4: Simulating and Characterizing Lattice Variability: This chapter outlines the computational framework for simulating lattice stiffness and discusses the properties of simulated lattices with varying levels of manufacturing noise and variability.

Chapter 5: Framework for Analyzing Test Accuracy: Test accuracy is determined for different prediction methods when applied to various groups of simulated lattices. These prediction methods are also applied to the stiffness data collected in Chapter 2.

Chapter 2

Mechanical Behavior of Physical Lattices

2.1 Cellular and Continuum Solids Models

The lattice structures used in this work have cellular microstructures, as do many naturally occuring materials such as wood, cork, and bone. These materials are often used in engineering applications for their high strength-to-weight ratios. Two-dimensional cellular solids include honeycombs, while three-dimensional cellular solids include the foams of Figure 1-2 and the lattice structures used in this work. Examples of lattice unit cell geometries include the simple cubic, octet truss, and rhombic dodecahedron structures shown in Figure 2-1.

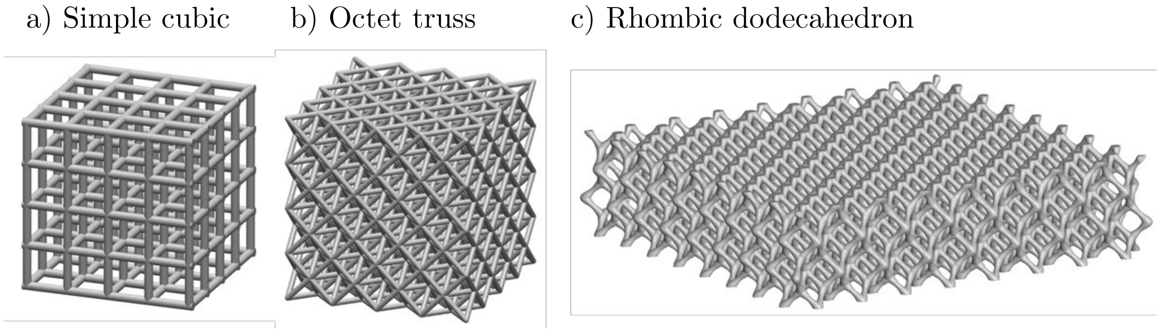
a) Simple cubic b) Octet truss c) Rhombic dodecahedron

Figure 2-1: Three dimensional lattice geometries are based off of repeated unit cell geometries: a) simple cubic, b) octet truss, and c) rhombic dodecahedron.

Continuum models represent the cellular structure as a homogeneous solid with equivalent properties. Along with the unit cell's geometry and the material properties of the bulk solid, the relative density drives many of the cellular solid's properties [5, 27, 28]. The relative density represents the volume fraction of the unit cell, or the density of the structure divided by the material's bulk density. Analytically this is given by

$$\rho_{\text{unit}} = \frac{\rho_{\text{eff}}}{\rho_{\text{solid}}} = \frac{nA_cL}{V_{\text{unit}}} \tag{2.1}$$

where n = number of edges per unit cell, A_c = cross-sectional area of a cell's edge, L = edge length, and V_{unit} = volume of the unit cell, including air. n and V_{unit} depend on the unit cell geometry, while L changes with the size of the unit cell. A_c depends on the manufacturing method and the desired cross section. Strut cross sections of AM midsoles are approximately circular with radius r_0, giving $A_c = \pi r_0^2$. Equation 2.1 then becomes

$$\rho_{\text{rel}} = \frac{n\pi L}{V_{\text{unit}}} r_0^2 \tag{2.2}$$

The unit cell's geometry governs the relationship between the relative density and the structure's effective properties. In this study, a rhombic dodecahedron structure was used in physical testing, while computational modeling used the octet truss lattice. An overview of the behavior of both structures is discussed in this section. Although bending of the rhombic dodecahedron lattice's struts dominate its behavior, the octet truss lattice is governed by axial stretching of the struts. As shown by Deshpande, Ashby, and Fleck in [19], a cellular structure is stretch-dominated when its unit cell meets Maxwell's criterion for static determinacy. In three dimensions, this criterion is given by $b - 3j + 6 \geq 0$, where b = number of struts and j = number of nodes in the unit cells. Deshpande et al. [19] also outlines conditions for structures with similarly situated nodes. In these structures the structure appears the same regardless of the orientation in which it is viewed. In three dimensions, these structures are stretch-dominated if they have node connectivity $Z = 12$. With a node connectivity of 12, the octet truss lattice satisfies this criterion and is stretch-dominated. The rhombic dodecahedron, by comparison, has a node connectivity of 8.

2.1.1 Rhombic Dodecahedron

The open-cell rhombic dodecahedron structure is bending-dominated with an effective elastic modulus which scales approximately with density squared (ρ^2) in all directions. As the name suggests, the unit cell is based on the space-filling convex polyhedron, as shown in Figure 2-2. A unit cell has 12 rhombic faces, giving it 24 edges and 14 vertices. This structure was analyzed by Babaee, Jahromi, et. al. in [7] and summarized here.

Rhombic dodecahedron unit cells have $V_{\text{unit}} = \frac{16L^3}{3\sqrt{3}}$. Together with Equation 2.1, this gives a relative density for the unit cell of

$$\rho_{\text{unit}} = \frac{9\sqrt{3}\pi r_0^2}{2L^2}$$

Edges in the rhombic dodecahedron structure are shared by three unit cells. This means that the relative density of the structure is a third of the unit cell density:

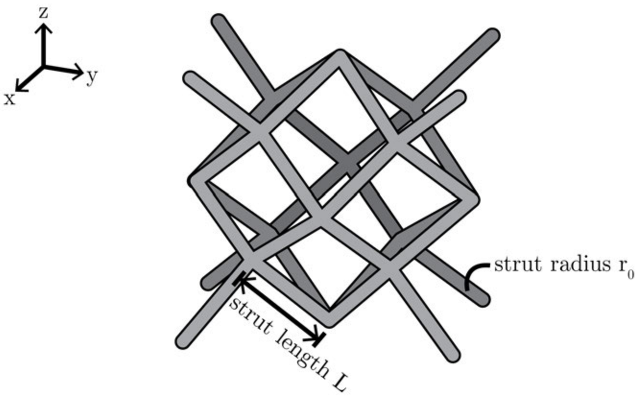

Figure 2-2: The rhombic dodecahedron unit geometry. Unit cells have 14 vertices and 24 edges with lengths L and radii r_0.

$$\rho_{\text{rel}} = \frac{\rho_{\text{unit}}}{3} = \frac{3\sqrt{3}\pi r_0^2}{2L^2} \tag{2.3}$$

The rhombic dodecahedron is has equivalent properties in both the y- and z-directions, defined by the axes in Figure 2-2. The x-direction corresponds to the the loading direction in running and is the relevant loading direction for this study. The effective elastic modulus in this direction, E_x is derived by calculating the strain energy during uniaxial compression and applying Castiglione's theorem, which is shown in detail in [7]. This is the only direction of interest in this study, and we will refer to E_x as E_{eff}. For a Young's modulus E_s of the bulk solid, this calculation gives

$$E_{\text{eff}} = \frac{1}{3\sqrt{3}} E_s \rho_{\text{rel}}^2 = \frac{3\sqrt{3}\pi^2}{4L^2}(E_s r_0^4) \tag{2.4}$$

In the rhombic dodecahedron lattice, E_{eff} scales with r_0^4 but only E_s, meaning E_{eff} is more sensitive to geometric changes in r_0 than material changes in E_s.

2.1.2 Octet Truss Lattice

The octet truss structure is based on a face-centered cubic unit cell, shown in Figure 2-3. To create the lattice structure, these octahedral unit cells are tesselated, with each strut shared between two cells. The unit cell and overall structure can also be described as a synthesis of tetrahedrons, as highlighted in Figure 2-3. An individual unit cell is represented by eight tetrahedrons. A full analysis of the octet-truss lattice's properties is shown by Deshpande, Fleck, and Ashby in [20].

The relative density of the octet-truss lattice is given by

$$\rho_{\text{rel}} = \frac{6\sqrt{2}\pi}{L^2} r_0^2 \tag{2.5}$$

The octet truss lattice has cubic symmetry.Modeling the structure as a pin-jointed

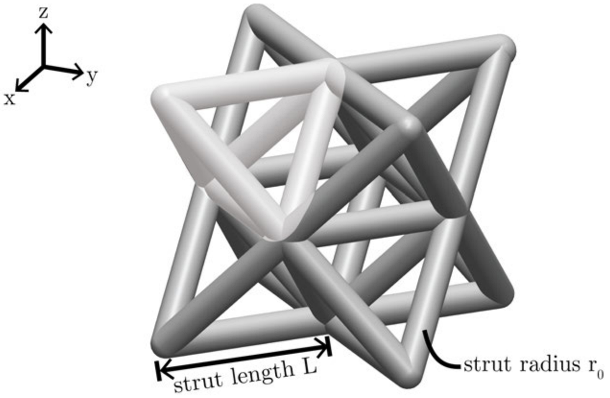

Figure 2-3: The octet truss unit cell geometry. The geometry is based off of the face-centered cubic unit cell but can also be described with tetrahedrons (highlighted).

Geometry	Relative Density, ρ_{rel}	Effective Elastic Modulus, E_{eff}
Rhombic Dodecahedron	$\frac{3\sqrt{3}\pi}{2L^2}r_0^2$	$\frac{1}{3\sqrt{3}}E_s\rho_{\text{rel}}^2 = \frac{3\sqrt{3}\pi^2}{4L^2}(E_s r_0^4)$
Octet Truss	$\frac{6\sqrt{2}\pi}{L^2}r_0^2$	$\frac{1}{9}E_s\rho_{\text{rel}} = \frac{2\sqrt{2}\pi}{3L^2}(E_s r_0^2)$

Table 2.1: Effective properties of the rhombic dodecahedron and octet truss lattices.

truss gives an effective modulus

$$E_{\text{eff}} = \frac{1}{9}E_s\rho_{\text{rel}} = \frac{2\sqrt{2}\pi}{3L^2}(E_s r_0^2) \tag{2.6}$$

Finite element models performed by Deshpande, Fleck, and Ashby in [20] showed a strong agreement between this relationship and observed results for octet-truss lattices of various densities.

For the octet truss lattice, E_{eff} scales with r_0^2 and E_s. As in the rhombic dodechaedron lattice, E_{eff} varies more with geometric changes in r_0 than material differences in E_s. However, the octet truss's effective modulus scales with r_0^2 instead of r_0^4, meaning it is less sensitive to changes in strut radius than the rhombic dodecahedron geometry. The relative densities and effective moduli for these two structures are summarized in Table 2.1. For both unit cell geometries, changes to strut geometry (r_0) or material properties (E_s) impact the effective modulus. This model holds for infinite-sized lattices. Due to their size and AM variability, it is not expected that the lattices used in this work perfectly follow these relationships.

2.2 Specimen Description

The objective of this work is to identify alternative tests that could potentially be used in a manufacturing environment to predict lattice stiffness. To represent the variability seen in production, known disturbances were introduced to create lattice specimens with material and geometric differences. A viable test determines differences in overall stiffness, not only those resulting from purely geometric or material changes.

Thirty specimens were printed on an M-series printer from Carbon at Carbon's headquarters in Redwood City, California, such as those in Figure 1-7. Specimens were printed using Carbon's proprietary EPU40, a light sensitive elastomeric polymer. EPU40 has a Young's Modulus E_s of 3.15 MPa and density of 1.025 g/cm^3 [8, 11]. Lattices had rhombic dodecahedron unit cells and measured nominally 80 mm x 80 mm x 20 mm overall with $(N_X, N_Y, N_Z) = (8, 8, 2)$ cells in each dimension. All specimens were printed from the same original file, but settings were modified on the printer to generate variability.

To capture material variability, fifteen samples were printed in each of two light intensities, denoted by "Group A" and "Group B." Group A had a lower light intensity level. Geometric variability was introduced by altering the blackline value, which represents a scaling of the strut thickness. A 0° blackline corresponds to an unaltered strut thickness. Negative values represent thicker struts, and positive values represent thinner struts. At least three samples were produced in each light intensity at each of four blackline values ranging from -120° to 120°. Each specimen in Group A and Group B had an identifying tag which listed its print ID, group ID (A or B) and blackline value.

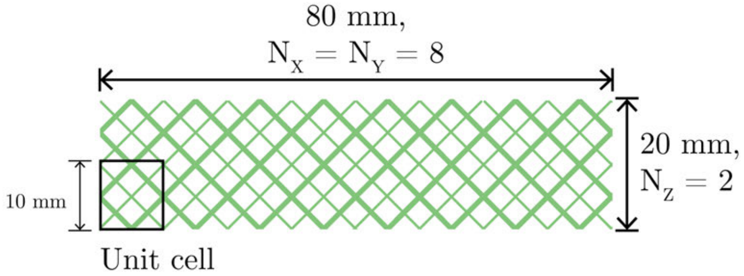

Figure 2-4: All mechanical tests in this thesis used rhombic dodecahedron lattices measuring 80 mm x 80 mm x 20 mm.

2.3 Experimental Setups

2.3.1 Stiffness

As described in Section 1.3.3, midsoles undergo quasi-static compression testing during production. Internal company test standards were adapted for this study to accurately determine the stiffness of the lattice puck samples used in this study and to accommodate available test equipment. Previous results from the Sports Technology course (see Section 1.4 and [15]) used a 25 mm cylindric indenter but produced inconsistent compression results with large uncertainty. Uncertainty on the order of 10% made it challenging to draw conclusions and correlate stiffness with the results of other test methods.

To improve repeatability and reduce uncertainty, samples were compressed between large compression platens. 150 mm diameter compression platens were mounted to a universal testing machine (model 5969) from Instron (Norwood, Massachusetts, USA) equipped with a 20 kN load cell, as in Figure 2-5. Lattice puck samples were placed on the lower platen and centered by eye. Samples were preloaded to 20 N instead of typical value used for full midsoles. The 20 N preload represents about 6-7% of the force at 10 mm compression flattened samples and remove any initial distortion. Other test parameters adapted from the existing in-line test and controlled through a test method written in Instron's Blue Hill software: the machine applied the preload at a rate of 75 mm/min, zeroed displacement, compressed the sample 10 mm at rate of 100 mm/min, and then rapidly returned to the neutral starting position.

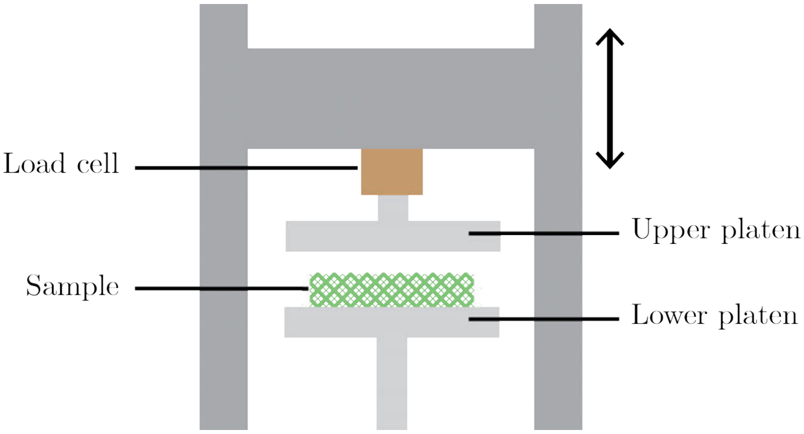

Figure 2-5: Diagram of Instron setup for lattice compression testing.

Each specimen was tested seven times with a 60 second recovery time between trials, which avoided capturing the material's cyclic viscoelastic response. The machine continuously recorded time, position, and force data during loading at a 1000 Hz sampling rate. All data was exported to comma-separated values (CSV) files after testing for further analysis in MATLAB (The Mathworks, Natick, Massachusetts, USA).

2.3.2 Mass and Volume

Mass and volume data were collected for the samples described in Section 2.2. Sample mass was measured using an AJ100 analytical balance from Mettler (Mettler-Toledo, Columbus, OH, United States), shown in Figure 2-6. The balance measures masses up to 110 g with 0.001 g resolution. Each sample was centered on the scale's plate prior to testing, and each sample was measured five times.

Figure 2-6: The AJ100 analytical balance used for lattice mass testing. Samples were centered on the plate, and mass was recorded with 0.001 g resolution.

The absolute volume of the lattice samples was determined using a water displacement test. A custom acrylic container with an interior cavity nominally measuring 1" x 3.5" x 5" (25.4 mm x 88.9 mm x 127 mm) was partially filled with enough water to completely cover lattices. After measuring the height of the water without a sample, a sample was submerged in the water. The height of the water was then recorded with the submerged lattice. All heights were measured to the bottom of the meniscus, as shown in Figure 2-7, using digital calipers with 0.01 mm resolution. Lattices were thoroughly dried between each of the three trials.

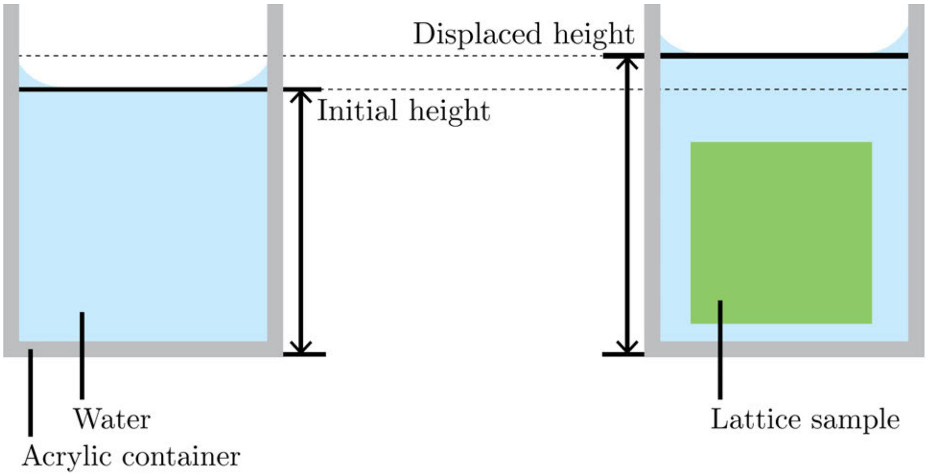

Figure 2-7: Lattice volume was determined through water displacement. Calipers were used to consistently measure water height to the bottom of the meniscus.

2.4 Results and Analysis

2.4.1 Stiffness

Custom MATLAB scripts imported and parsed the Instron CSV data, computed metrics for each trial, and averaged results across trials for each lattice specimen. Force-displacement graphs for all specimens and trials showed consistent shapes. These features derive from both the material properties of the bulk solid as well as the geometric properties of the lattice structure. Figure 2-8a shows force-displacement data for a representative sample. In the initial linear regime, lattice struts experience elastic loading. When struts reach their elastic limit, they buckle, creating a stress plateau. Once lattice struts buckle, they touch, and the structure reaches a densification point. The second linear elastic regime represents the compression of the solid material [27].

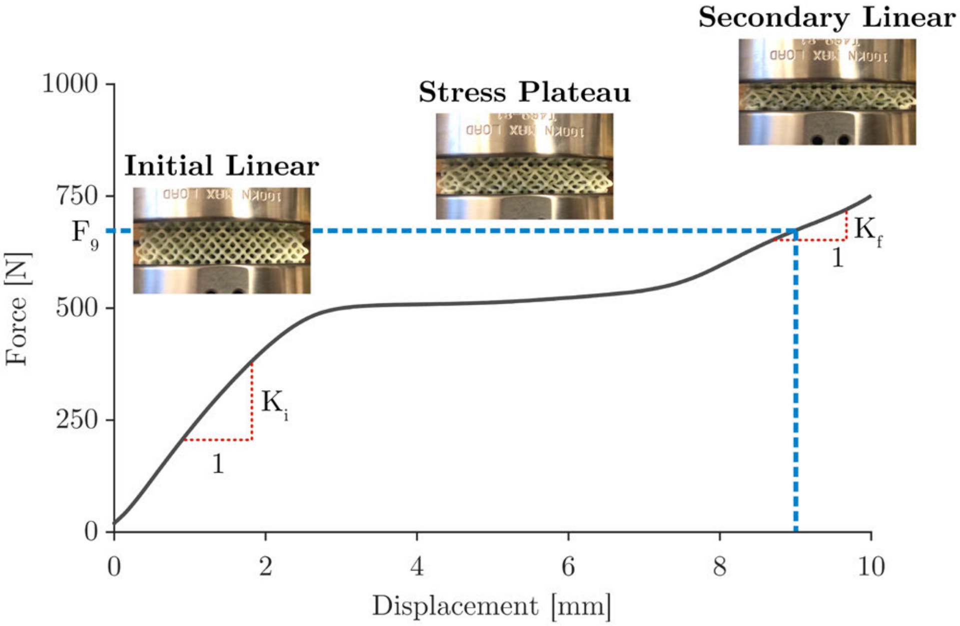

Figure 2-8: Force-displacement curves for 10 mm compression testing for all samples show similar features: an initial linear loading portion, in which struts begin to bend; a plateau, in which the lattice struts buckle; and a second linear portion. Key metrics include the slope of the initial and final linear regimes (K_i and K_f, respectively; shown in red) and the force at 9 mm compression (F_9; shown in blue).

These features occurred for all samples within each of its seven trials, but the first trial consistently produced higher forces from the last six trials, as shown in Figure 2-9. In practice, adidas performs a similar test once per midsole. High confidence in test method and fixturing means differences in results can be reasonably attributed to the midsoles rather than the test setup. Additionally, the long time required to perform this test (about one minute) makes it impractical to repeat in a manufacturing environment. adidas does not typically test lattices of this size, meaning we lack the same degree of confidence in this setup. Repeating the test allows us to obtain lower uncertainty by averaging across test repetitions.

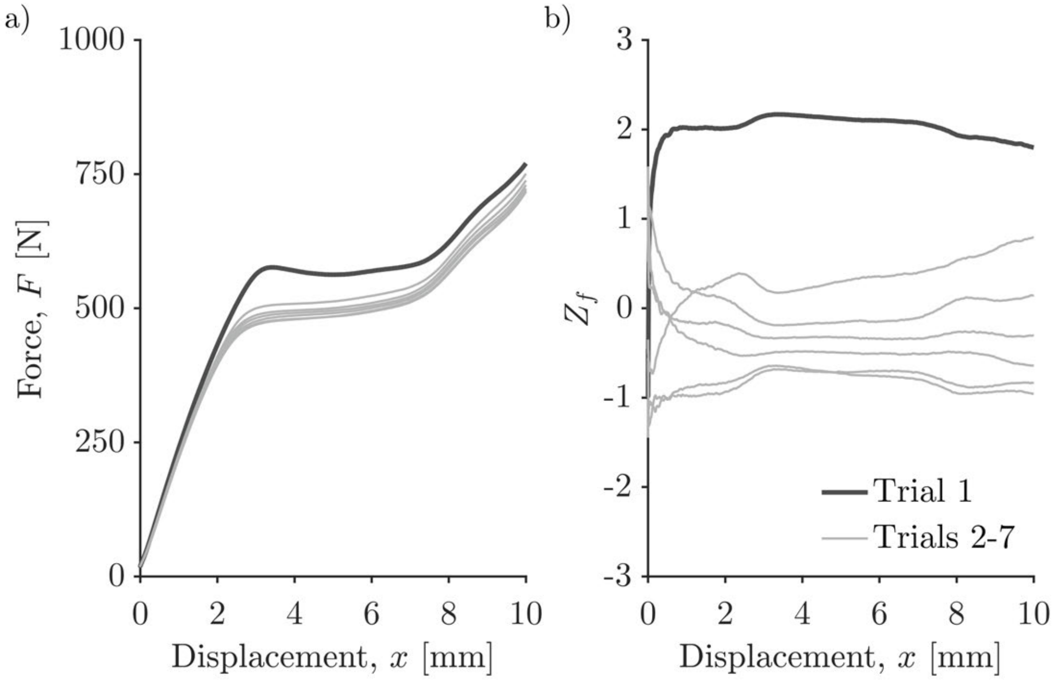

Figure 2-9: a) For all samples, loads were highest in the first trial (black) compared to the other six trials (grey) during a 10 mm quasi-static compression test. Data shown for a representative sample. b) Loads during the first trial were $\geq$ above two standard deviations from the mean force throughout the loading distance while forces for the other trials were ≤ 1 standard deviation from the mean. The first trial was excluded from further analysis. Data shown for same sample as a).

Due to its higher forces, the first trial was excluded from analysis for all samples. The standard deviation was used as a cutoff for justifying this. The standard deviation σ_f at each location x was determined for each sample across its seven trials. Z-scores were computed for each trial, representing the number of standard deviations of data from the mean; the difference $F(x,t) - \bar{F}$ was computed at each position x for each trial t and normalized by dividing by σ_f to give

$$Z_f(x,t) = \frac{F(x,t) - \bar{F}}{\sigma_f}$$

$Z_f(x,t)$ was computed for all trials. As shown in Figure 2-9b, $Z_f(x,t)$ was consistently at or above 2 for $x \geq 0.5$ mm, $t = 1$ for all samples. As a result, the first trial was excluded from further analysis, and metrics were only computed for trials $t \in [2, 6]$.

The existing quality control test uses force at 9 mm compression as a representation of midsole performance. Although this metric is easy to compute and consistent between trials, other metrics also characterize lattice behavior and correspond to relevant features of the loading curve shown in Figure 2-8. As a result, a variety of metrics were computed for each trial. Computed metrics included force at given displacements (1 mm increments ranging from 1 - 10 mm) as well as the average slope in the initial and final loading periods, shown in Figure 2-8. The initial linear regime was defined as displacements from 0 - 1.8 mm, and the final portion was defined as displacements from 8 - 10 mm. A first order polynomial fit ($y = ax + b$ was applied to each portion of the loading curve. The slope a of this fit represents the average stiffness K during that regime, in N/mm.

Figure 2-10 displays the average initial and final stiffnesses (K_i and K_f, respectively) as well as the force at 9 mm compression (F_9) for all samples. These outputs are compared to the blackline value and colored by light intensity group to confirm the impact of geometric (blackline) and material (light intensity) changes on overall lattice stiffness. Lattices with a more negative blackline value have thicker struts and are stiffer. Differences in light intensity or curing can result in a bulk solid with different material properties, resulting in samples with different stiffnesses.

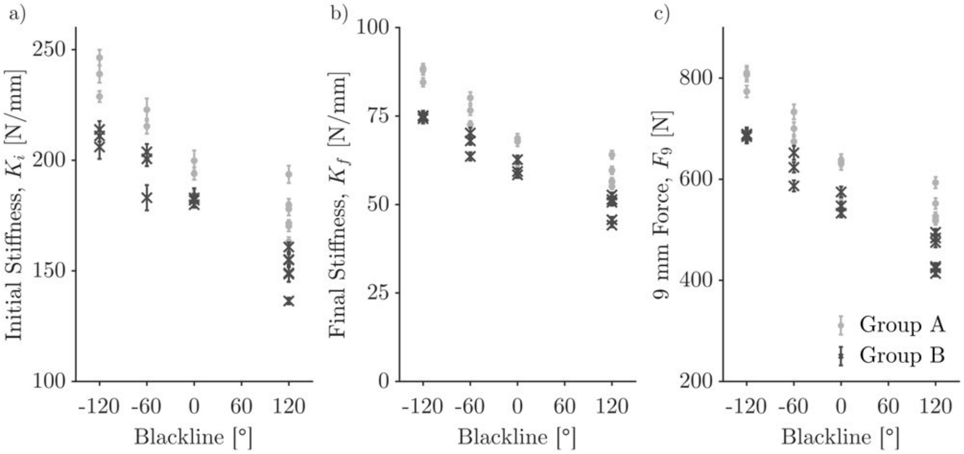

Figure 2-10: All stiffness metrics (K_i, K_f, and F_9) decreased with increasing blackline and was lower for light intensity Group B than for Group A. For samples printed with the same blackline and light intensity, initial stiffness shows greatest variability.

A two-way analysis of variance (ANOVA) was performed between blackline and material group, and results are included in Figure 2.2. There were significant main effects for both blackline value and material group ($p < 0.05$), but interaction effects were insignificant ($p = 0.48 > 0.05$) This confirms the hypothesis that both geometric (blackline) and material changes (light intensity) independently impact overall lattice stiffness. Geometric process parameters were responsible for a greater proportion of variance with an omega-squared of 0.716 compared to the omega-squared for material group of 0.129. This matches the analytical model of Table 2.1, in which geometric changes contribute more variability to effective stiffness than material changes. It is reasonable, however, that more severe differences in light intensity could result in greater variation due to light intensity.

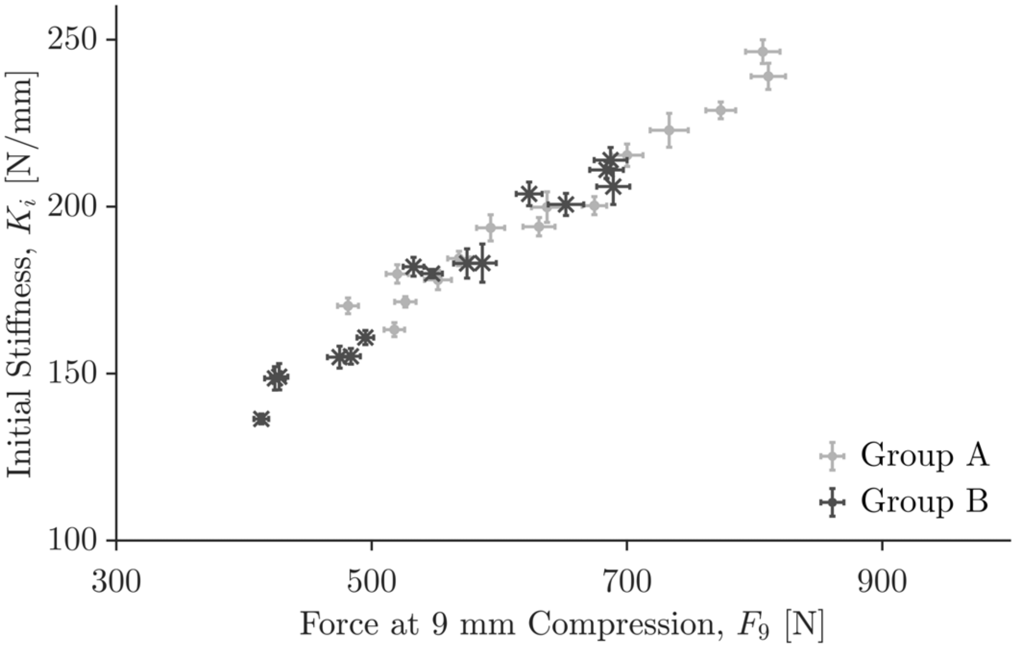

Figure 2-11: Average stiffness during the initial linear regime shows a strong correlation with the force at 9 mm of compression. Both metrics are representative of midsole stiffness.

2.4.2 Mass and Volume

Average mass for each sample was determined by averaging the seven mass measurements. Trial-to-trial measurements were variability, with an average fractional uncertainty of 0.030% between each sample's measurements[1]. As a result, the uncertainty in mass is small compared to the point size when comparing mass to other parameters, and error bars were omitted when generating figures for the mass, as in Figure 2-12.

Specimen volume was computed by finding the average change in water height,

---

[1] Unless otherwise specified, all uncertainties in this text represent 95% confidence levels.

	DF	Sum Sq	Mean Sq	F-value	P-value	η^2_{prop}	ω^2
Blackline	1	278000	278000	250.9	0	0.906	0.716
Light Intensity	1	50900	50900	46.0	0	0.639	0.129
Blackline × Intensity	1	563	563	0.51	0.482	0.019	-0.001
Error	26	28800	1110				
Total	29	357000					

Table 2.2: Two-way ANOVA results confirm impact of both geometric (blackline) and material (light intensity) changes on overall lattice stiffness.

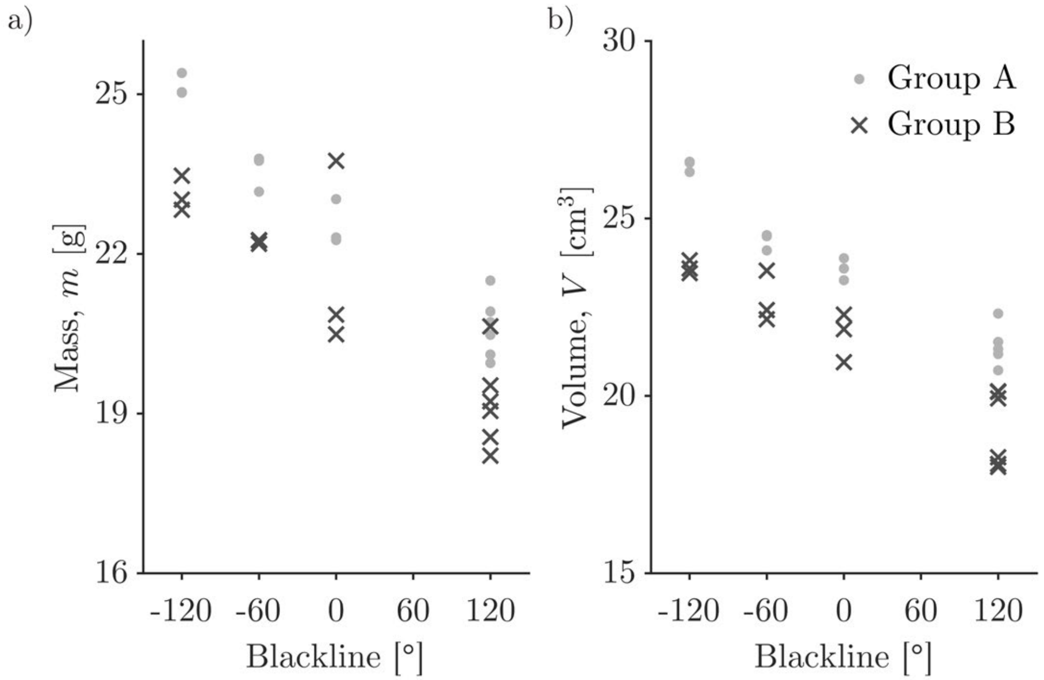

Figure 2-12: Increasing blackline reduces strut width, producing lattices with lower masses and less solid volume.

Δh, across the three measurements. The volume of the displaced water equals the volume of the lattice and is given by $V_L = \Delta V = wl\Delta h$, where w and l represent the width and length of the inside of the acrylic tank. The volume measurements resulted in an average fractional uncertainty of 9.2%, which represents the error in using calipers to accurately record water height to the bottom of the meniscus. Additional measurements for each lattice and/or more precise measuring equipment could further reduce volumetric uncertainty.

As with stiffness, both mass and volume decrease with increasing blackline values and are generally lower for group B compared to group A, as shown in Figure 2-12. However, the mass and volume show greater variance within each combination of blackline and light intensity.

Mass and volume show a strong positive correlation, as evidenced in Figure 2-13. Although local density variation within lattices is not captured through this method, these results suggest that individual samples have similar overall densities. The overall density of each sample was computed, and the average densities were not statistically different between the two material groups ($\rho_A = 0.964 \pm 0.021$ g/cm^3, $\rho_B = 0.994 \pm 0.038$ g/cm^3). With 99% confidence, the average density across all samples ($\rho = 0.979 \pm 0.026$ g/cm^3) matches the EPU40's advertised density of 1.025 g/cm^3 from Carbon [11].

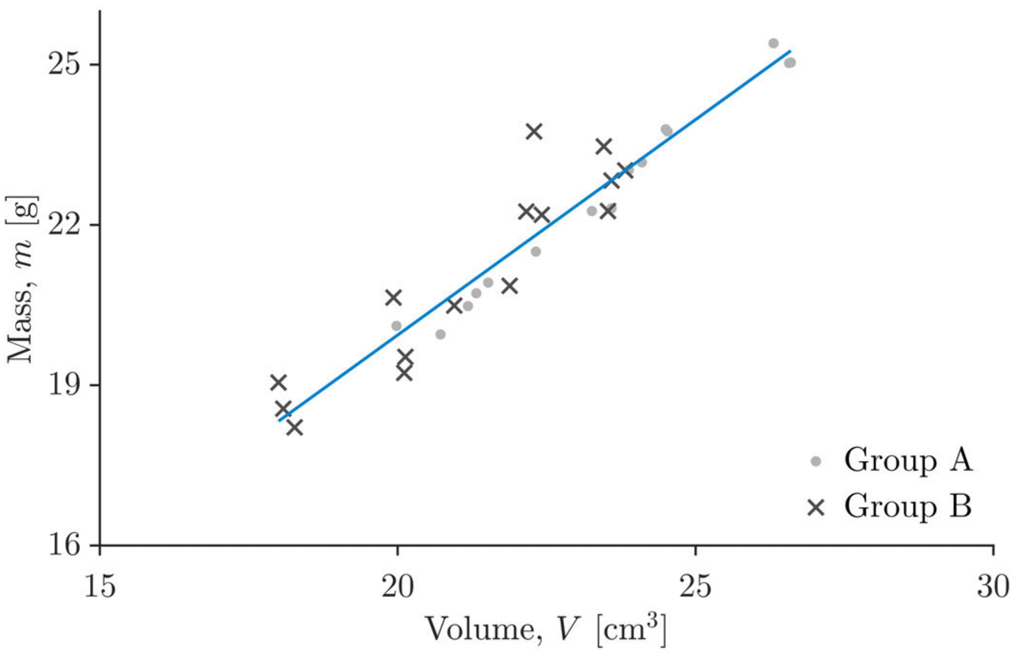

Figure 2-13: Sample mass increases linearly with volume of solid material. Sample density is represented by the ratio of mass/volume and is similar for all samples. Average material density is 0.979 ± 0.026 g/cm^3 and represented by the blue line ($y = 0.979x$). This agrees with Carbon's advertised density of 1.025 g/cm^3 [11].

2.5 Discussion

Stiffness shows a strong positive correlation with mass, as represented in Figure 2-14. Lighter lattices are less stiff, and heavier lattices are stiffer. This matches the analytical model of Table 2.1, which shows that the effective Young's modulus of a rhombic dodecahedron lattice scales with relative density squared. Since the material density is statistically the same for the lattices, as shown in Figure 2-13, both mass and volume are good indicators of the lattice relative density and thus stiffness. Measuring mass is more repeatable, making it an excellent predictor of overall stiffness. A proportional fit was applied to each light intensity group ($y = ax$, with adjustable slope a and 0 intercept). The slope fit parameters were not statistically different between the two light intensity groups (A: 28.4 ± 1.5 N/mm/g, B: 26.4 ± 1.6 N/mm/g), and the fit was re-computed across both groups, giving a slope of 27.5 ± 1.1 N/mm/g. The two light intensities used did not generate statistically different populations, but it is possible that larger differences in light intensity could result in samples with different stiffness-mass relationships.

Mass and stiffness can both be modeled as normally distributed random variables. The univariate quantile-quantile (QQ) plots in Figure 2-15 display the theoretical quantiles from a normal distribution and the actual quantiles of the sample data, represented by the black points. These points agree well with the grey line, confirming the assumption of normality. A bivariate QQ plot comparing the quantiles of the

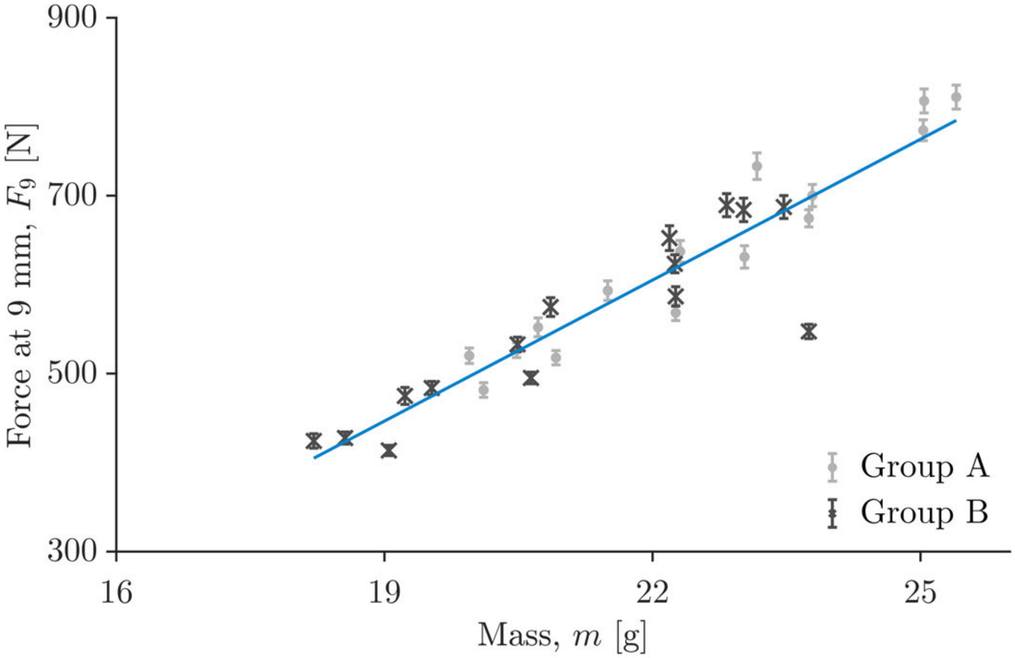

Figure 2-14: Stiffness increases linearly with sample mass for both light intensity groups. Proportional fits ($y = ax$) are not statistically different between the two light intensity groups. A proportional fit was re-computed across all samples with slope of 27.5 ± 1.1 N/g, represented by the blue line.

stiffness data with those of the mass data also shows a linear relationship, indicating that we can reasonably construct a bivariate Gaussian probability distribution function (PDF) from the physical data.

The linear regression shows that lattice stiffness increases with mass, and the QQ plots demonstrate that this relationship can be represented by a bivariate normal distribution. This physical data for $n = 30$ lattices suggests that mass could be used to predict overall lattice stiffness, although it is difficult to know whether 30 lattices accurately capture the wide range of variability found in AM. Chapter 5 presents a framework for analyzing the accuracy of various test methods and discusses in more detail the use of mass as a stiffness-prediction tool.

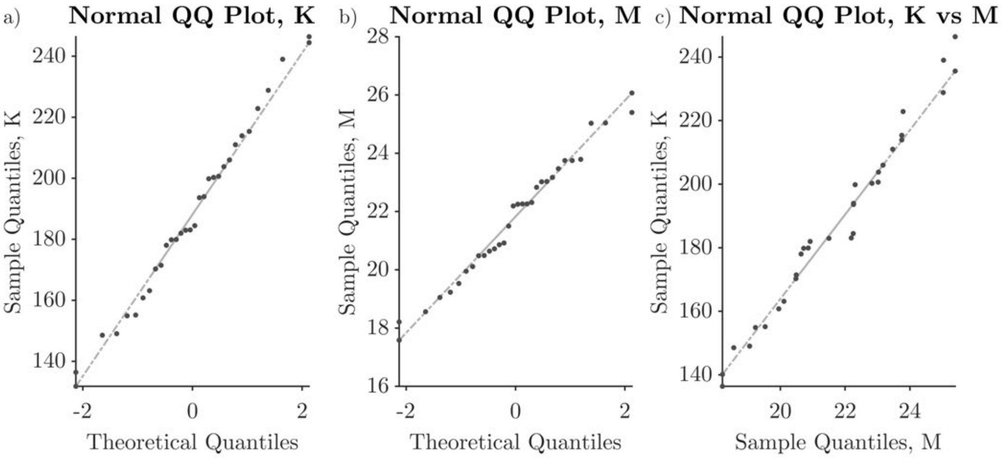

Figure 2-15: Quantile-quantile plots confirm the normality of mass and stiffness data. The distributions (y-axis) of stiffness (a) and mass (b) data agree well with the theoretical quantiles (x-axis) of the normal distribution. This is represented by agreement between the black points and the grey line. The stiffness quantiles also agree well with the mass quantiles in c), confirming bivariate normality.

Chapter 3

Acoustic Properties of Lattice Structures

3.1 Ultrasonic Testing Theory

Acoustic waves transfer mechanical energy without mass transfer by causing discrete particles to oscillate. These vibrations create a pressure wave with longitudinal oscillations, or oscillations in the direction of the wave's travel. We hear sound when this longitudinal wave transmits oscillations to our ears and causes the ear drum to vibrate. The human ear can detect frequencies between approximately 20 Hz and 20 kHz, and sound waves with frequencies exceeding 20 kHz are classified as ultrasonic.

A sound wave traveling through a material may be theoretically represented by a system of oscillating masses connected by elastic springs, as shown in Figure 3-1 [42]. The behavior of the mass-spring system is described by Hooke's Law: within the elastic limit of the material, restoring forces on particles have magnitude proportional to their displacements. As a wave travels through the spring system, particles will move; the speed of the wave as it travels depends on the material properties, such as the stiffness of the springs, but is independent of the magnitude of the wave applied. The wave's amplitude corresponds to the magnitude of the force experienced by a

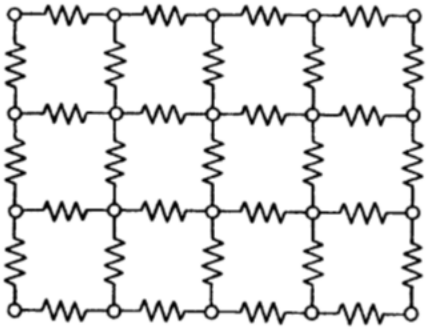

Figure 3-1: Model of an elastic body represented as system of masses and springs [42].

particle but does not impact the speed of sound within the material. The speed of sound instead depends on the material's mass, which corresponds to its density, and its spring constant, which relates to its elastic properties. This relationship is given as

$$V = \sqrt{\frac{C_{ij}}{\rho}}, \tag{3.1}$$

where V = speed of sound, C_{ij} = elastic constant, and ρ = density. The value of the elastic constant depends on the type of wave, and the ij subscript indicates its directionality; for anisotropic materials, the speed of sound will depend on both the type of wave and its direction of travel. For longitudinal waves in solids, the elastic constant C_{ij} from Equation 3.1 takes the form of the Young's Modulus in that direction [42, 6]. Equation 3.1 then becomes Young's Modulus in direction 1

$$V_1 = \sqrt{\frac{E_1}{\rho}}, \tag{3.2}$$

where E_1 is the Young's Modulus and V_1 is the speed of sound in direction 1. Although this relationship can be further described using the Poisson's ratio and Lamé constants, the form of Equation 3.2 is convenient for further analysis in this work.

3.1.1 Reflection and Transmission

Acoustic impedance describes the resistance a sound wave experiences when traveling through a material. As a wave travels, it produces a pressure gradient in the material, generating stress and strain and causing particles to move. Acoustic impedance relates this motion within a material to the pressure it experiences. Analytically, acoustic impedance is characterized by the speed of sound V and density ρ and is represented by Z, where

$$Z = V\rho \tag{3.3}$$

Materials with higher density or speed of sound will provide more resistance to a sound wave. As a result, materials with high acoustic impedance are described as acoustically hard while those with low impedance are called acoustically soft [6].

When a wave reaches a boundary, the acoustic impedance changes. This causes part of the wave's energy to reflect toward the source and part of it to continue without a change in direction. In an ideal material, sound pressure decreases only as a result of wave spread. Real materials are not strictly homogeneous, which creates interfaces where materials of different density and/or sound velocity meet. This means the materials show attenuation; the magnitude of a wave decreases as it travels in a material as some of the wave's energy is reflected at inhomogeneities.

The acoustic impedance on either side of a boundary governs how much of the incident wave is transmitted and how much is reflected. The coefficients of reflection, R, and transmission, D, represent the ratio of sound pressure of the reflected and transmitted wave to the ratio of the original wave:

$$R = \frac{p_r}{p_e} \quad \text{and} \quad D = \frac{p_d}{p_e}$$

p_r and p_d are the sound pressure of the reflected and transmitted waves, respectively, and p_e is the sound pressure of the incident wave. We can then derive

$$R = \frac{Z_2 - Z_1}{Z_2 + Z_1} \quad \text{and} \quad D = \frac{2Z_2}{Z_2 + Z_1}. \tag{3.4}$$

where Z_1 and Z_2 are the acoustic impedances of the initial and second materials, respectively. Combining with Equation 3.3 with Equation 3.4 gives

$$R = \frac{\rho_2 V_2 - \rho_1 V_1}{\rho_2 V_2 + \rho_1 V_1} \quad \text{and} \quad D = \frac{2\rho_2 V_2}{\rho_2 V_2 + \rho_1 V_1}. \tag{3.5}$$

The energy reflection coefficient is given by

$$\frac{\text{Reflected energy}}{\text{Incident energy}} = R^2 \tag{3.6}$$

while the energy transmission coefficient is given by

$$\frac{\text{Transmitted energy}}{\text{Incident energy}} = \frac{Z_1}{Z_2} D^2 \tag{3.7}$$

When $Z_1 \ll Z_2$, $R \to 1$. The energy reflection coefficient R^2 also approaches 1. Meanwhile, $\frac{Z_1}{Z_2} \to 0$, and the energy transmission coefficient approaches 0. Almost all of the wave is reflected, and only a small amount of the incident wave's energy is transmitted to the second material.

3.1.2 Pulse-Echo Testing

Pulse-echo testing is a specific form of ultrasonic testing which uses reflected sound waves to characterize samples. In practice, pulse-echo testing is often used to identify cracks or other defects in stiff materials. A transmitter produces an ultrasonic pulse, which spreads into the specimen and is reflected to the receiver. In a traditional analog setup, a pulse generator sends an electric pulse to the transmitter, and the receiver transforms the reflected signal into an electric signal before sending it to a cathode ray (CR) tube. Modern setups are digital and utilize analog-to-digital (AD) converters instead of the CR tube.

Several display options are frequently used for this type of ultrasonic testing. One technique, called the A-scan, represents the reflected ultrasonic pulse as a single peak on a graph comparing sound amplitude (y-axis) with time (x-axis). Although part of the reflected wave enters the receiver, part of it changes direction, reflecting and returning toward the test specimen. The continuing cycle of reflection off of the backwall and the sensor produces subsequent echo peaks on the display read out.

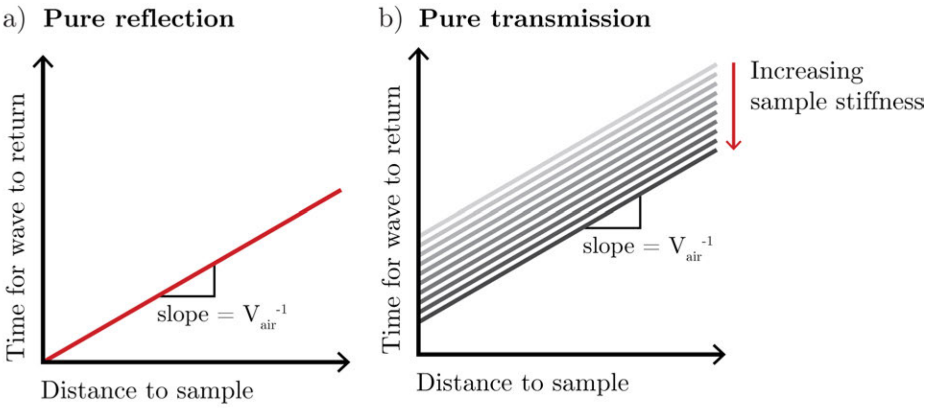

Figure 3-2: As the sensor moves away from an object, the time it takes for the wave to travel through air increases. This is represented by a line with slope equal to the inverse of the speed of sound, V_{air}^{-1}. In a), the wave reflects off of the object. When there is no separation between the sensor and sample, the hypothetical time for the wave to return is zero, and the line has zero intercept. In b), sound is transmitted to the sample. The positive intercept represents the time it takes for the sound to travel through the sample, and the magnitude of the y-intercept depends on sample stiffness.

Due to both transmission of wave energy to the receiver and attenuation within the test material, these peaks will decrease in amplitude and ultimately approach zero.

Ultrasonic range finding sensors use the pulse-echo method to determine distance between the sensor and an acoustically hard object. This type of sensor includes a transmitter, which sends a burst of ultrasonic waves, and a receiver, which records when the burst returns. The sensor transmits a pulse width modulation (PWM) signal. The length of the PWM signal represents the delay in time between sending receiving the wave burst. This time delay response represents the time for the signal to travel to and from an acoustically hard material. As a result, the recorded time equals the time for the sound wave to travel to and from the object:

$$t = \frac{2d}{\bar{V}}, \tag{3.8}$$

where d is the distance between the sensor and target object and $\bar{V}$ is the average speed of sound. When the wave only travels through air before reflecting, $\bar{V} = V_{\text{air}}$. This relationship is summarized as a proportional fit with slope $= 2V_{\text{air}}^{-1}$ and zero intercept, as in Figure 3-2a.

When the sound wave travels through air as well as the lattice material, $\bar{V}$ represents the average speed of sound through both the lattice and the air. Equation 3.8 becomes

$$t = 2(t_{\text{air}} + t_{\text{sample}}), \tag{3.9}$$

where

$$t_{\text{air}} = \frac{d}{V_{\text{air}}} \quad \text{and} \quad t_{\text{sample}} = \frac{H}{V_{\text{sample}}} \tag{3.10}$$

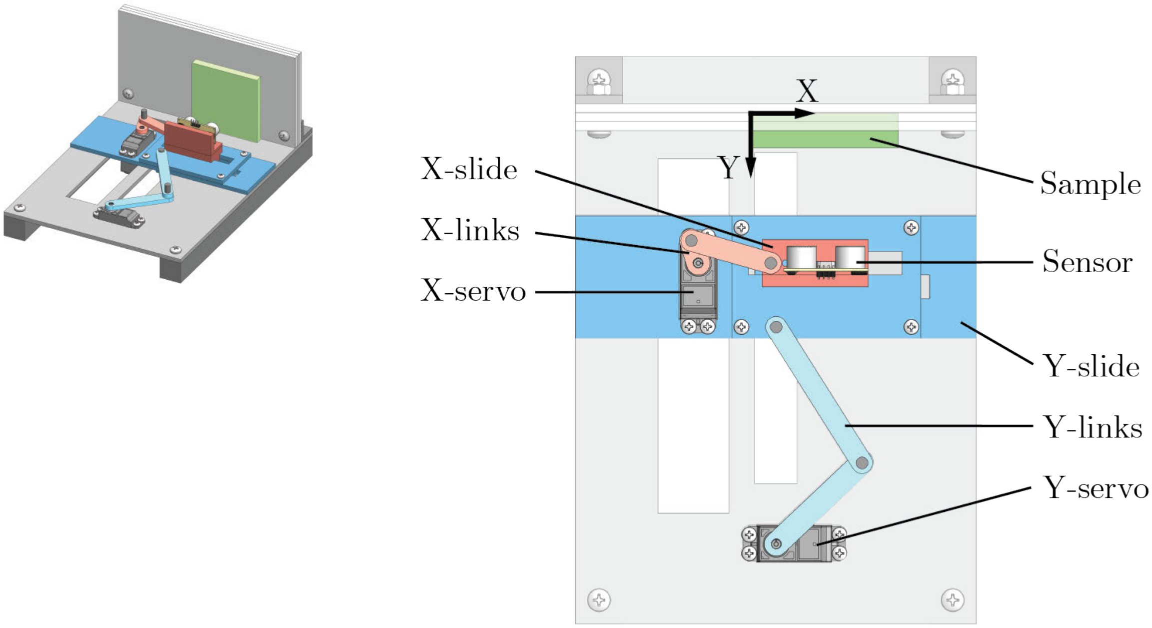

Figure 3-3: Labeled diagram of the two-axis apparatus used to control the position of the ultrasonic sensor during data collection.

This results in a a linear relationship between response time and the distance between the sensor and the sample, as represented in Figure 3-2b. As in Figure 3-2a, the slope has magnitude $2V_{\text{air}}^{-1}$; however, the non-zero intercept represents the time it takes the sound to travel through the material and is given by $2HV_{\text{sample}}^{-1}$. From Equation 3.2, the speed of sound in a solid can be related to its Young's Modulus and density. Combing Equations 3.2, 3.9, and 3.10 gives

$$t(d, E) = \frac{2d}{V_{\text{air}}} + \frac{2H\sqrt{\rho}}{\sqrt{E}} \tag{3.11}$$

Equation 3.11 can also be related to the sample's mass, geometry, and spring constant via

$$\rho = \frac{m}{AH} \quad \text{and} \quad E = \frac{kH}{A} \tag{3.12}$$

Together, Equations 3.11 and 3.12 become

$$t(d, m, k) = \frac{2d}{V_{\text{air}}} + 2\sqrt{\frac{m}{k}} \tag{3.13}$$

3.2 Apparatus

A pulse-echo testing device was designed to test the stiffness of different lattices. The apparatus, shown in Figure 3-3, consisted of a fixed mounting plate to secure the sample and a two axis linear stage to move the ultrasonic sensor.

Lattice samples fit into a fixed plate so that sound waves travel through the lattice's Z-dimension, as defined in Section 2.2. This corresponds to the direction of loading that would occur in a running shoe midsole and matches the direction of loading in the existing compression test. The samples, nominally 80 mm x 80 mm x 20 mm fit snuggly in an acrylic panel with a cutout measuring 77 mm x 77 mm x 10 mm. The undersized cutout compressed the samples slightly but did not preload the samples enough to visually distort the sample or cause warping.

Two VS-2A servo motors (Vigor Precision Limited, Hong Kong) controlled the position of the ultrasonic sensor in the X- and Y-directions. As defined in Figure 3-3, the X-axis represents lateral position across the face of the sample, and the Y-axis represents movement toward and away from the lattice. Slider-crank mechanisms converted the rotary motion of the servo to straight-line motion of the X-axis stage, highlighted in dark blue, and of the sensor mount, highlighted in red. Links were sized to allow 25 mm of X-direction travel and 100 mm of Y-travel.

The two servo motors and the ultrasonic sensor were controlled by an Arduino Nano 3.0 from Gravitech (Minden, NV, USA). The HC-SR04 ultrasound sensor (Cytron Technologies, Johor, Malaysia) sends a burst of ultrasonic waves and records the time it takes for the burst to return to the sensor [1, 22]. To do this, the Arduino sends a 10 μs TTL (transistor-transistor logic) signal to the sensor. This initiates a burst of eight 40 kHz waves. At time $t = 0$, the sensor finishes releasing the waves. The wavefront first travels through air to reach the sample, represented in Figure 3-4. At time $t = t_{\text{air}} = dV_{\text{air}}^{-1}$, the waves reach the face of the sample. Under the transmission model, the waves enter the lattice sample and continue to propagate until they reach the acoustically hard acrylic backing material. At time

$$t = t_{\text{air}} + t_{\text{sample}} = \frac{d}{V_{\text{air}}} + \frac{H\sqrt{\rho}}{\sqrt{E}},$$

the waves reflect off of the backing material. The waves then return to the sensor, traveling first through the sample and then through the air, ultimately returning to the sample at time

$$t = t_{\text{delay}} = 2(t_{\text{air}} + t_{\text{sample}}) = \frac{2d}{V_{\text{air}}} + 2\sqrt{\frac{m}{k}},$$

according to Equation 3.13. Upon receiving this wave burst, the ultrasonic sensor sends a pulse width signal to the Arduino with width t_{delay}.

The HC-SR04 has a 3 mm specified distance resolution, corresponding to a time resolution of 17.5 μs. The sensor works best over distances of 20 mm to 5 m. At distances under 20 mm, interference between the initial wave burst and the returning waves becomes significant, and results become unreliable. Waves propagate from the sensor at an enclosed angle of 30°. At a measuring distance of d, this means waves spread $d \tan \frac{\theta}{2}$ in any direction, where θ represents the enclosed angle. The HC-SR04 sensor was centered vertically (Z-direction as indicated in Figure 3-4). The maximum distance between the sample and the sensor was set at 150 mm. At this distance, waves from the sensor spread about 40 mm in each direction. This corresponds to

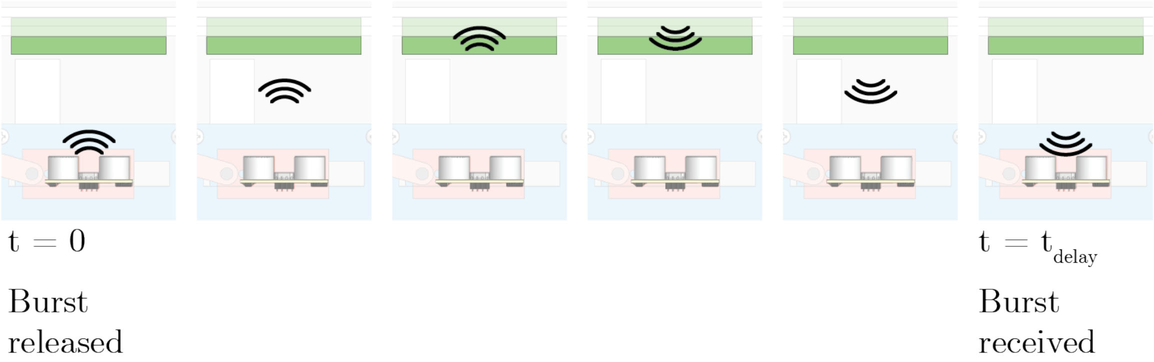

Figure 3-4: Schematic representing the progress of the sound wave during the pulse-echo testing used in this study.

half the length of the sample and avoids undesired reflection of sound waves off of the apparatus.

3.3 Method

The ultrasonic testing apparatus of Section 3.2 was used to measure delay times for eight samples at each of five X positions and each of ten Y positions, for a total of 50 positions. One sample was tested from each of the four blackline levels and the two light intensity groups described in Section 2.2. The sensor moved through the full range of X positions before moving to the next Y position and returning to the initial X location. At each of the fifty locations, the ultrasonic sensor performed 200 testing cycles at a frequency of approximately 80 Hz. A serial connection relayed t_{delay} for each measurement to a computer, where it was exported to CSV at the end of each trial. Five trials were collected for each sample.

3.4 Results

MATLAB scripts imported and parsed the CSV data for each trial. Data were averaged across the 200 measurements at each (X,Y) position for each trial. The fractional uncertainty from averaging across these 200 measurements averaged $1.59 \pm 0.06\%$. This reflects the consistency between individual measurements within a single trial, and this uncertainty from this averaging was neglected in future computations.

The averaged delay time at each location is shown in Figure 3-5 for a representative sample. The small grey points represent each location's average value. There was no statistically significant trend between delay time and X position, and results for each Y position were averaged across the five X positions. These averages are represented by the larger grey points in Figure 3-5 for one sample or the points in Figure 3-6 for all samples.

The delay time increases as the sensor moves away from the sample. This matches the analytical models for both transmission and reflection of the sound waves: with

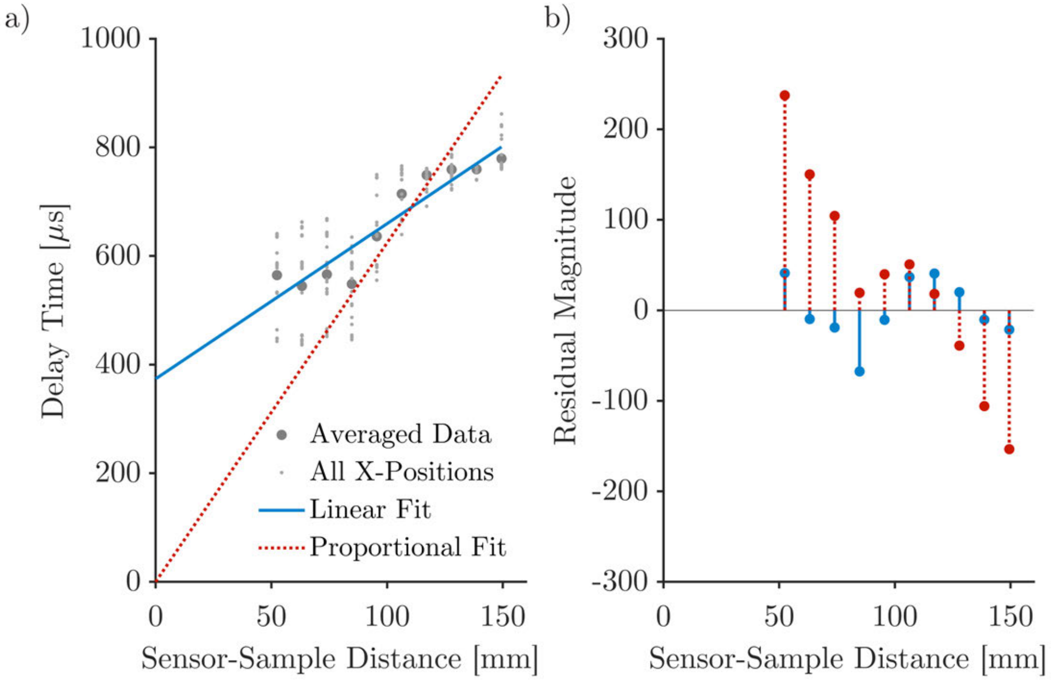

Figure 3-5: a) Time values at each distance are shown along with the linear (blue, representing transmission) and proportional (red, representing pure reflection) fits. b) Residuals at each distance for both fits. The systematic variation of the proportional fit's residuals suggesting that this model does not describe data well. Residuals for the linear fit are randomly distributed, suggesting that the transmission model better describes data.

increasing distance, it takes longer for waves to travel to and from the lattice sample. This is true regardless of whether sound waves are transmitted to the lattice or simply reflect off of its face. To confirm that sound waves are transmitted to the sample, linear and proportional fits were computed for each sample across the full ranging distance of 50 mm to 150 mm. For each sample, all measurements at a given Y position were used to compute the two fits. Residuals were also determined for the two fits across the entire ranging distance. Residuals from the proportional fit revealed a poor agreement with the data, as shown in Figure 3-5. The residuals from the proportional fit show systematic variation, decreasing linearly with the testing distance. The linear model better describes the data. The residuals from the linear fit are more randomly distributed, suggesting that the linear model better describes the data. The linear fit matches the transmission model of Equation 3.13, where the slope of the line corresponds to the speed of sound in air, and the intercept relates to the time it takes for sound to travel through the lattice sample. The proportional fit, however, only makes sense if no sound is transmitted to the lattice.

The analytical model predicts parallel linear fits for each sample, where the slope of the linear fit corresponds to the inverse of the speed of sound in air. This is constant regardless of the lattice's stiffness. Under this model, the fit slope should show no statistically significant trend with lattice stiffness. The values of the slope do not

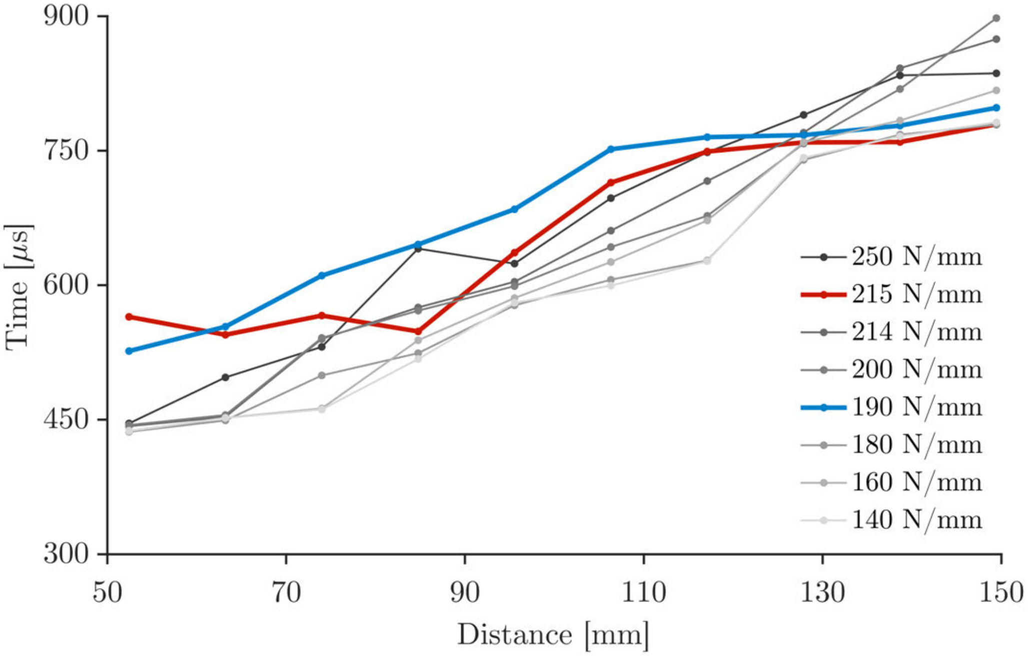

Figure 3-6: Overview of time response for all samples as a function of distance between the sample and the sensor. Time delay increased with separation distance, and stiffer samples generally had longer time responses. Samples with statistically different fit parameters are shown in red and blue.

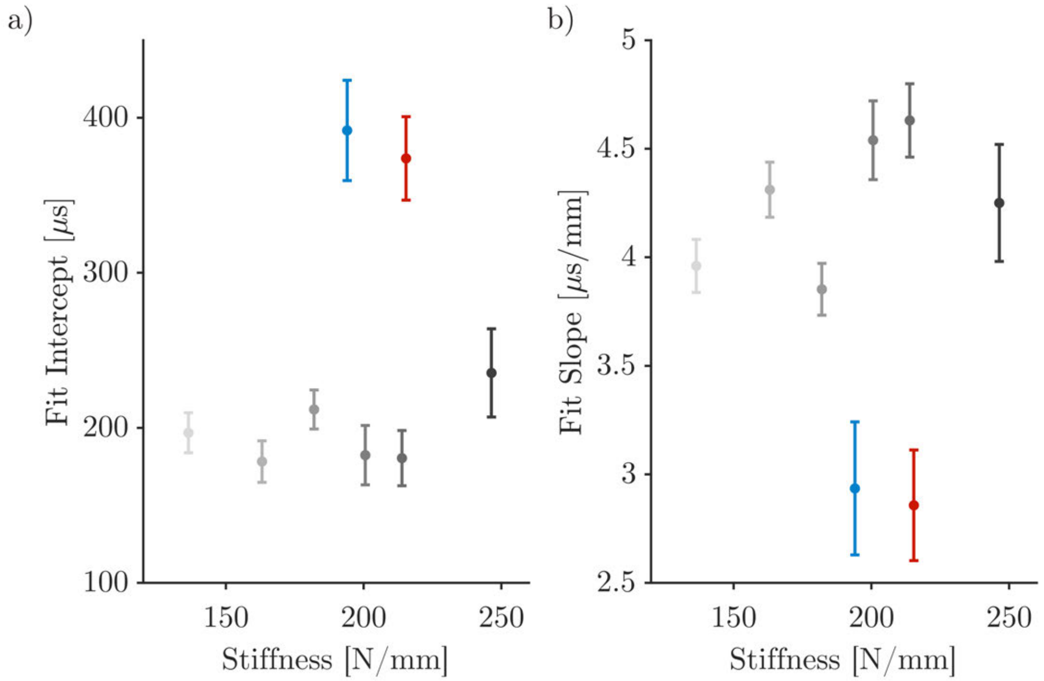

Figure 3-7: Both linear fit parameters from the ultrasonic distance, a) intercept and b) slope, show little correlation with sample stiffness. The analytical model predicts a slope which is independent of stiffness. The model predicts an intercept which decays with $\frac{1}{\sqrt{k}}$, but this relationship is not observed.

match the model, which predicts a slope of 5.8 μs/mm. The magnitude of this value could reflect some inaccuracy in the ultrasonic sensor.

The fit's intercept corresponds to lattice's effective stiffness. We expect to see intercepts which scale with $\sqrt{k^{-1}}$, or $\sqrt{mk^{-1}}$ when normalized for lattice mass. This means that the fit intercept should decrease with increasing lattice stiffness, which is not the trend found, represented in Figure 3-7. Scaling the x-axis of Figure 3-7 to normalize mass does not reveal additional trends.

Although the fit intercept is approximately 200 μs for six of the eight samples, two samples have much higher intercepts of approximately 400 μs. Removing these two samples still does not yield a clear visible (or statistical) trend between intercept and stiffness. This could be an artifact of the ultrasonic sensor's resolution. Another possibility is that the samples tested have stiffnesses which are too similar to distinguish with this form of ultrasonic testing.

We expect linear fits to produce parallel lines with different y-intercepts. The y-intercept of this fit across the entire distance yields the most physically meaningful result, corresponding to the modeled behavior of Equation 3.13. However, this is not the only way to analyze different results between samples. The vertical distance between samples's time responses in Figure 3-6 at a given sensor position also represents this information. The speed of sound and testing distance does not change, meaning differences in measured time response can be attributed to different speeds of sound

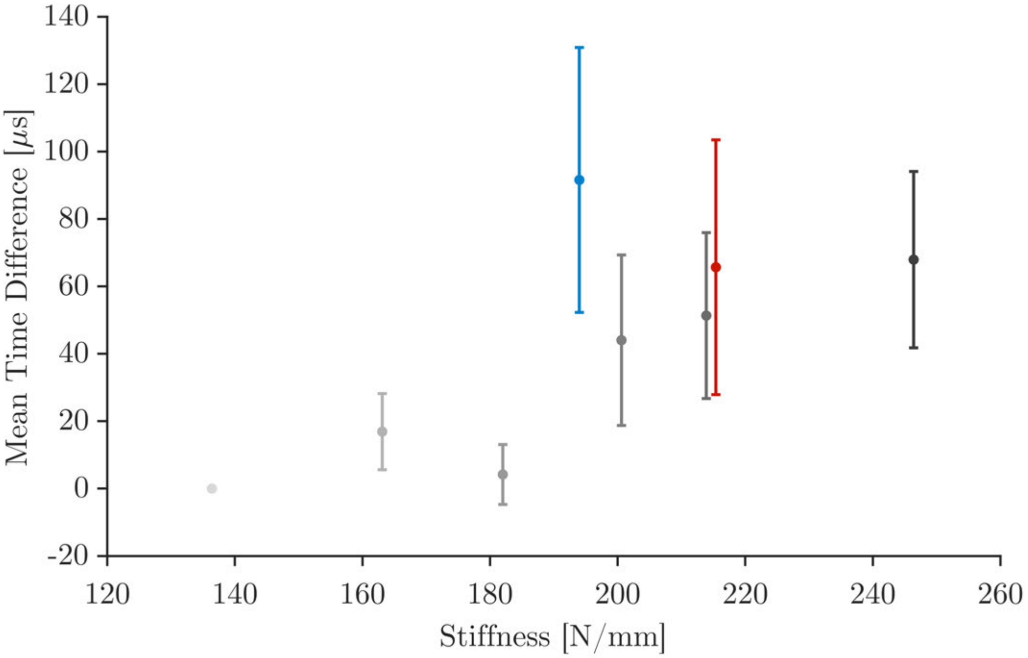

Figure 3-8: At each position, the difference was computed between each sample's time response and that of the least stiff sample. When averaged across the entire testing distance, these time differences show a positive correlation with sample stiffness. Although two samples (in red and blue) had statistically different linear fit parameters, all samples follow this trend. The trend is statistically significant with $p = 0.0398 < 0.05$.

in the samples. At each testing distance, the difference in time delay between each sample and the least stiff sample was computed. Averaged across the entire ranging distance, this represents the average vertical distance between the data points of different samples. From the physical model, we expect the least stiff sample to have the highest time values, and stiffer samples will have progressively smaller time values. Though we see the opposite of this trend in Figure 3-8, the results are statistically significant.

A linear regression ($y = ax + b$) of the data in 3-8 produces statistically significant fit parameters, $a = 0.75 \pm 0.70$ μs/N/mm and $b = 162 \pm 37$ μs. Despite a high fractional uncertainty, this initial data shows a statistically significant trend between lattice stiffness and this offset value, with $p = 0.0398 < 0.05$. Additional data could potentially lower the high fit uncertainty or reveal other trends that cannot be statistically determined from the low ($n = 8$) sample count.

3.5 Discussion

Acoustic testing offers the potential for a rapid and inexpensive test. Data acquisition with the current apparatus takes approximately four minutes per sample. This is largely driven by collecting 200 measurements taken at each of five x-positions; however, the 200 measurements were usually very similar to each other, and there was no statistically significant relationship between time response and x-position. Reducing both the number of x-positions and the number of measurements at each position would decrease testing time. Although the current test time is much longer than the current compression test, which takes about one minute per midsole, the components cost significantly less than a servohydraulic, universal testing machine, which can cost upwards of \$15,000. In total, the raw materials used to fabricate the device cost approximately \$20, and electronic components cost approximately \$40, with the Arduino Nano (approx. \$30) largely driving the cost. At scale, custom printed circuit boards could fabricated at a much lower cost.

Preliminary data collection of eight lattices with variable geometric and material properties shows that ultrasonic sound waves are successfully transmitted to the lattice samples. For all eight samples, the linear model, corresponding to transmission, matches data better than the proportional model, which represents reflection of the sound wave off of the front of the lattice. In reality, the sound is likely not purely reflected or transmitted. The ultrasonic sensor used only outputs one value, corresponding to the time it takes for an emitted wave burst to return to the sensor. Future work could explore other ultrasonic sensors, which might output more information about the waves received by the sensor over time. This would provide more information about transmission, reflection, and echo patterns of the lattice samples.

Sample stiffness has a statistically significant impact on the time delay, but the relationship does not correspond to the analytical model of expected behavior. This could be due to complex acoustic behavior of the soft lattice structures. As sound travels through the lattice, it passes through air and refracts through beams. This behavior may not be adequately captured by representing the lattice structure as a homogeneous, cellular solid. The disagreement with the analytical model could also result from sensor irregularities such as limited sensor resolution or nonlinear behavior with increasing distance from the sample. Although the linear fits were statistically significant with the HC-SR04 sensor used, a higher quality sensor would likely have less noise and more linear behavior, resulting in a higher statistical confidence in results.

Although sound waves are transmitted to the lattice structure and do not only reflect off of the front surface, most of their energy reflects off of individual struts. Acoustic impedance for air and EPU40 can be calculated from Equations3.3 and 3.1: $Z_{air} = 413$ Pa s/m and $Z_{EPU} = 56{,}800$ Pa s/m). Equation 3.4 gives a coefficient of reflection of 0.986, meaning almost all of the incident wave reflects off of an individual strut, and very little is transmitted to the strut itself. Previous work has modeled the effective refraction of cylinder arrays [29, 43, 35] by simulating the reflection of waves off of individual cylinders, known as a multiple scattering simulation. Additional work studies the impacts of void inclusions on the acoustic propereties of materials [24, 57, 60, 44]. Future work could focus on developing this scattering simulations for lattices with different geometric and material properties to determine whether and how this form of ultrasonic testing could capture effective lattice stiffness.

Ultrasonic testing of lattice samples could provide rapid, inexpensive information about lattice stiffness, but further work is needed. Additional data[1] should be collected for the remaining 22 lattice samples in order to better understand these trends and whether both geometric and material variability are captured by this form of ultrasonic testing.

---

[1] The original timeline for this thesis included plans to collect this data. Due to the spread of COVID-19 in Spring 2020, collecting additional data was not possible.

Chapter 4

Simulating and Characterizing Lattice Variability

4.1 Numerical Simulation

Beem, Fay, and Lilin's computational lattice solver from [9] was modified for use in this study. The simulation represents a lattice as a network of struts with connections at joints, as shown in Figure 4-1. The simulation tool solves for the force balances and constitutive equations in both static and dynamic loading cases. In static loading, the internal load ($\mathbf{f}_m$) in strut M between nodes i and j, as represented in Figure 4-1 is

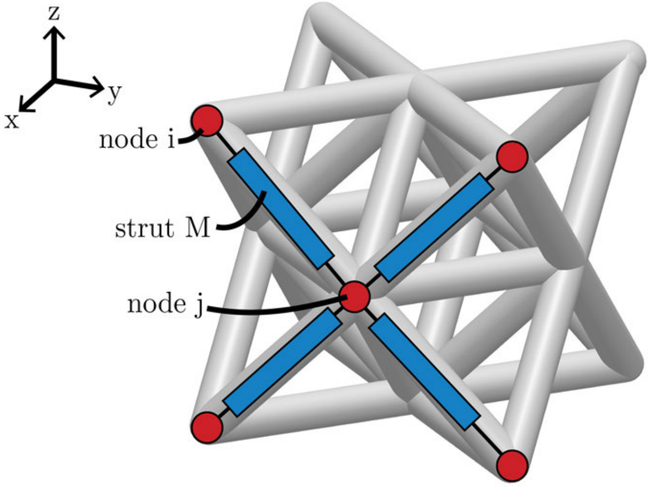

Figure 4-1: Octet truss unit cell with labeled with nomenclature from the numerical simulation: nodes i and j and strut M.

$$\mathbf{f}_m = \frac{\mathbf{r}_j - \mathbf{r}_i}{|\mathbf{r}_j - \mathbf{r}_i|} k_m (L_{0M} - |\mathbf{r}_j - \mathbf{r}_i|) \tag{4.1}$$

where $\mathbf{r}_i$ and $\mathbf{r}_j$ are positions of nodes i and j, k_M is the stiffness of strut M, and

L_{0M} is the initial length of the strut. As shown in equation 4.1, the internal forces depend on the lengths of the struts, represented by

$$L = \sqrt{(x_i - x_j)^2 + (y_i - y_j)^2 + (z_i - z_j)^2}$$

This nonlinear relationship between node positions (x_i, y_i, z_i) and (x_j, y_j, z_j) and strut forces requires a Newton solver for both static and dynamic cases. The Newton solver used in this study utilizes an implicit Generalized-Conjugate Residual (GCR) to solve each linear system without storing the Jacobian. Beem, Fay, and Lillin also developed Newton solvers which performed LU decomposition using the Jacobian method either by computation of finite differences or analytical stamping of the derivative of 4.1. For larger lattices, this implicit GCR method is up to 10 times faster and uses up to 25 times less memory than these methods. The general outline of the Newton solver with GCR is:

```
$l \leftarrow 1$, $\mathbf{x}^k \leftarrow$ initial guess;
repeat Newton Loop
    Evaluate $\mathbf{F}(\mathbf{x}^k)j \leftarrow 0, \mathbf{p}^j \leftarrow -\mathbf{F}(\mathbf{x}^k)$;
    repeat Implicit GCR loop: solve
        $\mathbf{J}_F[\mathbf{x}^k]\Delta\mathbf{x}^{k+1} = -\mathbf{F}[\mathbf{x}^k]$ for $\Delta\mathbf{x}^{k+1}$;
        Compute
          $\mathbf{J}_F(\mathbf{x}^k)\mathbf{p}^j = \frac{1}{\epsilon}(\mathbf{F}(\mathbf{x}^k + \epsilon\mathbf{p}^k) - \mathbf{F}(\mathbf{x}^k))$;
        Orthonormalize in the image space;
        Update solution and residual $\mathbf{r}^j$
    until $\|\boldsymbol{r}^j\|/\|\boldsymbol{r}^0\|$ small;
    $x^{k+1} \leftarrow x^k + \Delta x^{k+1}; k \leftarrow k + 1$
until $\|\boldsymbol{F}(\boldsymbol{x}^{k+1})\|, \|\boldsymbol{x}^{k+1}\|$ small;
```

Figure 4-2: Algorithm for Newton solver with implicit GCR [18].

In order to determine the relationship between lattice mass and stiffness, Beem, Fay, and Lillin's numerical solver [9] was modified to create localized mass concentrations and introduce noise.

To represent more extreme cases of manufacturing variability, lattices were created with the same overall mass but varying mass concentrations. An $m \times n \times p$ boolean tensor T represented an $N_X \times N_Y \times N_Z$ lattice as an array of unit cells. Each T_{ijk} represented whether or not to scale all struts in a given unit cell $(x, y, z) = (i, j, k)$, with $x \in \{1, 2, \ldots, N_X\}, y \in \{1, 2, \ldots, N_Y\}, z \in \{1, 2, \ldots, n_Z\}$. Struts in unit cell ijk are scaled when $T_{ijk} = 1$. Tensor T with

$$T_{ijk} = 1 \text{ for } i \in \{1, 2, ..., N_X\},\ j \in \{1, 2, ..., N_Y\},\ k = 1,\ 0 \text{ elsewhere}$$

scales only the lowest vertical layer of the lattice. A T with

$$T_{ijk} = 1 \text{ for } i \in \{1, 3\},\ j \in \{1, 2, \ldots, N_Y\},\ k = \{1, 2, \ldots, N_Z\},\ 0 \text{ elsewhere}$$

scales two slices of unit cells: those at $x = 1$ and those at $x = 3$.

The radii of all struts in unit cell ijk were set to $r = r_0(1 + \delta_C T_{ijk})$. Struts shared between two unit cells were scaled if either of the adjacent cells was scaled. After scaling all struts in this manner, the entire lattice volume was normalized such that $\sum \frac{r^2}{r_0^2} = 1$. This ensured the generated lattices had the same overall mass but different mass concentrations.

Two types of noise were added to lattices in order to represent more typical variability seen in a manufacturing environment. First, individual strut radii were scaled by either Gaussian noise with $(\mu, \sigma) = (0, \delta_S)$ or uniform noise across interval $(a, b) = (-\delta_S, \delta_S)$. This noise represents local differences between struts due to random variation within production of a single lattice. To represent variability between production of different parts, all of a lattice's strut radii were scaled either by Gaussian noise with $(\mu, \sigma) = (0, \delta_L)$ or uniform noise across interval $(a, b) = (-\delta_L, \delta_L)$. δ_S, δ_L, and the type of noise (either Gaussian or uniform) could be easily modified to represent different types of variability.

The process for generating a lattice with mass concentrations and noise is represented in Figure 4-3

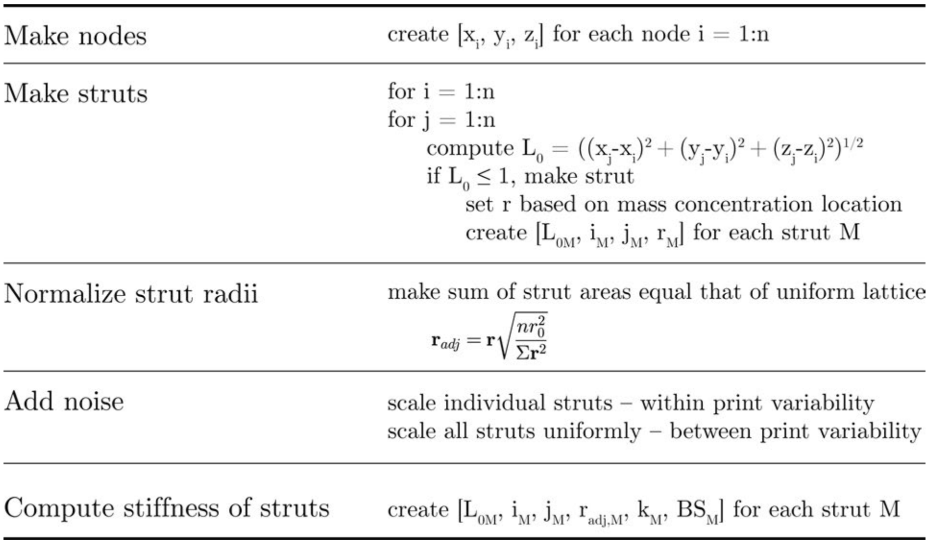

Make nodes

```
create $[x_i, y_i, z_i]$ for each node i = 1:n
```

Make struts

```
for i = 1:n
for j = 1:n
    compute $L_0 = ((x_j-x_i)^2 + (y_j-y_i)^2 + (z_j-z_i)^2)^{1/2}$
    if $L_0 \leq 1$, make strut
        set r based on mass concentration location
        create $[L_{0M}, i_M, j_M, r_M]$ for each strut M
```

Normalize strut radii

```
make sum of strut areas equal that of uniform lattice
    $\mathbf{r}_{adj} = \mathbf{r}\sqrt{\frac{nr_0^2}{\Sigma \mathbf{r}^2}}$
```

Add noise

```
scale individual struts – within print variability
scale all struts uniformly – between print variability
```

Compute stiffness of struts

```
create $[L_{0M}, i_M, j_M, r_{adj,M}, k_M, BS_M]$ for each strut M
```

Figure 4-3: Schematic of numerical solver's process to generate lattice parameters.

The effective Young's modulus of the lattice structure is most easily determined through pure axial loading. A lattice's theoretical effective modulus (derived in Section 2.1 and summarized in Table 2.1) derives corresponds to its behavior in the initial loading regime, such as in Figure 2-8. In this region, behavior is controlled by the bending and stretching of the lattice struts [28]. Due to the small size of the lattices used here, we do not expect agreement with the infinite-sized model; behavior under large displacement is more relevant for the potential application. Boundary conditions were set on each face: the two X and Y planes were free in all directions, and the lower Z face was fixed at zero displacement in all directions. The upper Z face was fixed at zero displacement in the X and Y directions and experienced a fixed load in the -Z direction.

4.2 Analytical Spring Model

A simplified spring model was used to understand the impact of concentrated mass on overall lattice stiffness. Although random noise does occur during manufacturing to produce struts of different sizes, manufacturing could also produce lattices with regions where struts are uniformly sized differently. The most realistic scenario is mass concentrated in the lower portions of a lattice. After printing, samples are placed on drying racks for washing and curing. Uncured liquid resin on a sample would collect on the lower lattice struts, where it would cure during later processes. This scenario can be modeled as vertically stacked layers of material with different stiffnesses, as represented in Figure 4-4 by four springs in series.

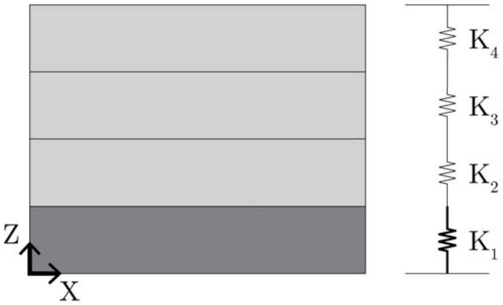

Figure 4-4: Representation of a lattice as a composite with various stiffness layers, equivalent to springs in series, where each layer represents a layer of unit cells. Increasing the strut radii in layer $z = 1$ increases stiffness K_1 of that layer.

Each layer i has stiffness K_i, giving an effective stiffness K_e of

$$K_e^{-1} = \sum (K_i^{-1}) = K_1^{-1} + K_2^{-1} + K_3^{-1} + K_4^{-1} \tag{4.2}$$

Each layer is a cellular solid representing the homogenized octet truss lattice and has stiffness

$$K_i = \frac{E_i A_i}{L_i} \tag{4.3}$$

where A_i is the cross section of the solid's contact face, L_i is the height of the layer, and E_i is the effective stiffness of the cellular solid layer. Each layer of the composite cellular solid has the same area $A_i = L_x L_y$ and height $L_i = L_z$. Combined with Equation 2.6, which gives the effective modulus of an octet truss lattice with bulk modulus E_s, strut radii r_i, and strut length l, this gives a layer stiffness of

$$K_i = \left(\frac{6\sqrt{2}\pi E_s}{9l^2}\right)\left(\frac{L_x L_y}{L_z}\right) r_i^2 \tag{4.4}$$

Equation 4.4 can also be related to the stiffness of the uniform lattice with radius r_0 and stiffness K_0:

$$K_i = K_0 \left(\frac{r_i}{r_0}\right)^2 \tag{4.5}$$

To normalize lattice mass, the sum of the strut cross sections in a modified lattice is set equal to that in the nominal, unchanged lattice. For the four-layered example, this means

$$4r_0^2 = r_1^2 + r_2^2 + r_3^2 + r_4^2 \tag{4.6}$$

A lattice with a single layer scaled by factor β has $r_1 = \beta r_0'$ and $r_2 = r_3 = r_4 = r_0'$. Lattice mass is normalized after adding scaling struts and thus adding additional mass. In order to maintain the same overall mass, this means the "unchanged" struts will be thinner than the struts in the uniform lattice after normalization. Applying Equation 4.6 for this scenario yields

$$r_0' = r_0\sqrt{\frac{4}{3+\beta^2}}, \tag{4.7}$$

$$r_1 = r_0\beta\sqrt{\frac{4}{3+\beta^2}}, \tag{4.8}$$

and

$$r_2 = r_0\sqrt{\frac{4}{3+\beta^2}} \tag{4.9}$$

As β represents a positive scaling factor by which to increase mass, $\sqrt{\frac{4}{3+\beta^2}}$ will always be less than 1, meaning $r_2 < r_0$, as described above. When $\beta = 1$, representing no scaling, $r_1 = r_2 = r_0$. We substitute the r_1 and r_2 values from Equations 4.8 and 4.9 into Equation 4.5 to give

$$K_1 = K_0\beta^2\left(\frac{4}{3+\beta^2}\right) \tag{4.10}$$

and

$$K_2 = K_0\left(\frac{4}{3+\beta^2}\right) \tag{4.11}$$

$K_2 = K_3 = K_4$ means Equation 4.2 becomes $K_e^{-1} = K_1^{-1} + 3K_2^{-1}$, where

$$K_e = K_0\left(\frac{4}{3+\beta^2}\right)\left(\frac{\beta^2}{1+3\beta^2}\right) \tag{4.12}$$

If a lattice instead has two layers which are scaled by factor β, $r_1 = r_2 = \beta r_0'$ and $r_3 = r_4 = r_0'$. Applying Equation 4.6 to this configuration results in

$$r_0' = r_0\sqrt{\frac{2}{1+\beta^2}}, \tag{4.13}$$

$$r_1 = r_0\beta\sqrt{\frac{2}{1+\beta^2}}, \tag{4.14}$$

and

$$r_2 = r_0\sqrt{\frac{2}{1+\beta^2}} \tag{4.15}$$

As before, we substitute the r values from Equation 4.14 and 4.15 to give

$$K_1 = K_2 = K_0\left(\frac{2\beta^2}{1+\beta^2}\right) \tag{4.16}$$

and

$$K_3 = K_4 = K_0\left(\frac{2\beta^2}{1+\beta^2}\right) \tag{4.17}$$

$K_1 = K_2$ and $K_3 = K_4$ means Equation 4.2 becomes $K_e^{-1} = 2K_1^{-1} + 2K_2^{-1}$, where

$$K_e = K_0\left(\frac{\beta^2}{(1+\beta^2)^2}\right) \tag{4.18}$$

Evaluating Equations 4.12 and 4.18 for $\beta = 1.1$, or 10% scaling, gives $K_e = 0.248K_0$ for both the single and double scaled layer scenarios. The uniform lattice has $K_e = 0.25K_0$. At $\beta = 1.2$, or 20% scaling, $K_e = 0.244K_0$ for the single layer and $K_e = 0.242K_0$ when two layers are scaled. Modifying strut radii in localized regions should create lattices with the same overall mass but different stiffness. Additionally, greater levels of systematic variation (either higher β levels or more regions which are scaled) cause larger decreases in the structure's effective stiffness.

4.3 Specimen Description

Lattices were generated with the same overall size $(N_X, N_Y, N_Z) = (5, 5, 4)$, unit cell size (10 mm, as in Figure 2-4), bulk modulus (3.15 MPa), and bulk density (1.025 g/cm^3). Lattices were generated for each geometric mass concentration and combination of noise and scaling factors. Six concentrations, shown in Figure 4-5 were created to represent potential variability during manufacturing. Mass concentration tensors T were constructed for each of the six conditions, where a value of $T_{ijk} = 1$ means unit cell $(x, y, z) = (i, j, k)$ receives additional mass and is shaded dark grey in Figure 4-5. The "bottom" concentrations place additional mass at the bottom of the layers, the "center" concentrates additional mass in the middle of the lattice, and "side" explores the impact of stiffer columns in the direction of loading.

Lattices were created at each of ten noise levels ($\delta_s = \delta_L =$ 1.25-10%, in increments of 1.25%, set to Gaussian noise) and ten scaling factors ($\delta_c =$ 0-22.5%, in increments of 2.5%). Lattices with the scaling factor of 0% did not have localized mass concentrations but were affected by strut noise. 100 lattices were generated at each parameter combination, for a total of 60,000 lattices.

The numerical solver computed the lattice displacement at a fixed load of 120 N in the -Z direction. The displacement of the uppermost lattice nodes, along with lattice parameters such as mass, concentration location, scaling factor, and noise level were saved for additional analysis in MATLAB.

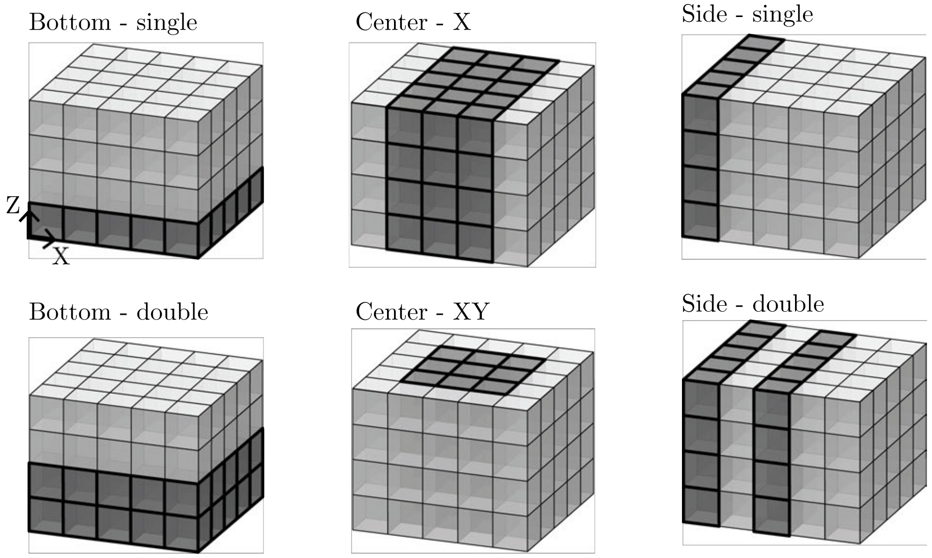
Bottom - single

Center - X

Side - single

Bottom - double

Center - XY

Side - double

Figure 4-5: Lattices were generated in each of six mass concentration geometries for a lattice with $(N_X, N_Y, N_Z) = (5, 5, 4)$. In this schematic, dark grey cells represent more dense regions while light grey cells are less dense with thinner strut radii.

4.4 Results and Analysis

The impact of concentrated mass is most noticeable at combinations of low noise levels with high scaling factors. Figure 4-6 shows all generated lattices from the lowest noise level and highest scaling factor. Each color represents a different concentration geometry from Figure 4-5, with $n = 100$ lattices in each geometry. Under these conditions, variation is dominated by moving mass to different regions of the lattice. The samples for each geometry roughly cluster around parallel lines with different slopes. Including a small amount of noise variability demonstrates that increasing mass causes similar stiffness increases for all concentration locations.

The nominal mass and stiffness of the uniform, unchanged lattice (no noise or mass concentrations) are also included in Figure 4-6, represented by the dashed lines. All geometries have similar average masses, but all average stiffnesses are lower than the nominal lattice stiffness. This makes sense as the standard lattice geometry is well optimized for strength-to-weight ratio; we expect unevenly distributed mass to produce less stiff structures. At 20% scaling, the analytical model from Section 4.2

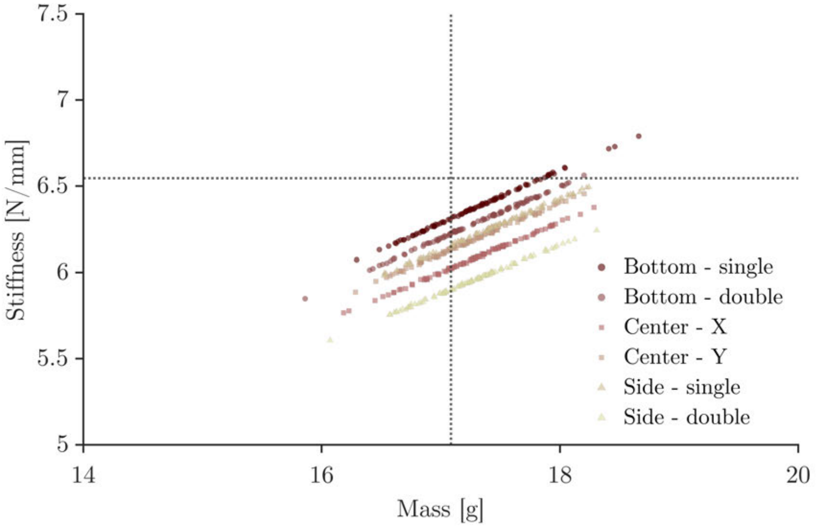

Figure 4-6: Generated lattices at 1.25% noise and 20% scaling, colored by location of the mass concentration. The horizontal and vertical lines represent the stiffness and mass of an unmodified lattice, respectively. Creating a mass concentration and adding a small amount of strut noise decreases stiffness in all geometries. All geometries show linear trends between mass and stiffness with similar slopes but different intercepts.

predicts that the single and double layer conditions ("Bottom - single" and "Bottom - double") will have 97.6% and 96.8%, respectively, of the effective stiffness of the unmodified lattice.The average stiffness of simulated lattices at 20% scaling is 6.37 N/mm (single layer) and 6.29 N/mm (double layer), compared to 6.55 N/mm for the uniform case. These represent 97.4% and 96.1% of the uniform stiffness, representing strong alignment with the simplified, analytical model.

"Bottom - single" and "Bottom - double" are the most probable conditions based on the physics of the printing and curing process; however, including the data for the other conditions as well as data for populations without additional scaling creates a "worst case" population of samples.

Stiffness variation due to strut noise is most easily visualized at 0% scaling, when all variation comes from this type of noise. As noise levels increase, the range of observed masses and stiffnesses increase, as shown in Figure 4-7. The average mass is unaffected by noise, as evidenced by points centered around the nominal mass of an unchanged lattice, represented by the dotted line. Increasing noise causes the average stiffness to decrease, with the population average moving farther from the predicted stiffness K_{pred} of the unchanged lattice. Higher levels of strut noise also create populations with greater stiffness variability: at a given mass, a wider range of stiffnesses are observed at higher noise levels. Although the blue points in Figure 4-7 were generated under different conditions from all of the points in Figure 4-6, both populations contain lattices with a range of stiffnesses for a given mass.

As with data for physical lattices, simulated behavior of the noisy, non-uniform lattices is normally distributed. Lattice populations were defined from all lattices

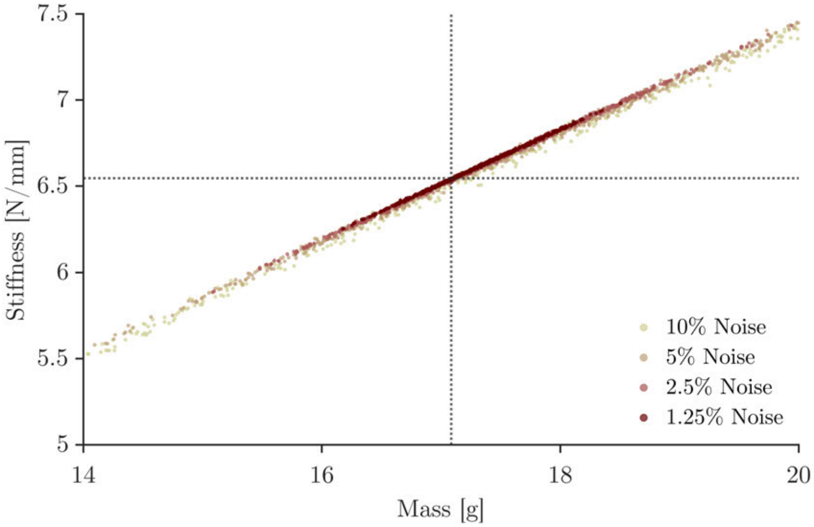

Figure 4-7: Generated lattices at all noise levels and 0% scaling, colored by noise level. The horizontal and vertical lines represent the stiffness and mass of an unmodified lattice, respectively. As noise increases, the range of mass and stiffness increase. At higher noise levels, stiffness shows greater variability.

created at a given combination of noise and scaling level, and bivariate Gaussian distributions were fit to each population. With $n = 100$ lattices generated at each of the six geometries in Figure 4-5, each population of lattices had 600 total lattices.

To generate the distributions, populations were centered around $(0, 0)$ and normalized by the population's average mass and stiffness. This produces inputs to the bivariate PDF of (m', k'), where m' and k' represent the fractional difference from the average mass and stiffness, respectively. This is given by

$$m' = \frac{m - \mu_m}{\mu_m} \quad \text{and} \quad k' = \frac{k - \mu_k}{\mu_k} \tag{4.19}$$

A k' value of 0.15 represents a stiffness of 15% above the population mean. This corresponds to mass-manufacture of AM lattice midsoles, where specification limits are defined based on athlete needs (percentages above and below mean stiffness), not based on the capabilities of the manufacturing lines.

The bivariate probability distributions of Figures 4-9 can be characterized in a number of ways. One technique is to generate confidence regions. For the bivariate PDF, the interval for probability p consists of vectors $\mathbf{x}$ where

$$(\mathbf{x} - \boldsymbol{\mu})^T \boldsymbol{\Sigma}^{-1} (\mathbf{x} - \boldsymbol{\mu}) \leq \chi_2^2(p) \tag{4.20}$$

Here, μ represents the two-dimensional mean vector and Σ represents the 2×2 covariance matrix. The chi-squared distribution with two degrees of freedom defines the interior of an ellipse. We can visualize 95% confidence regions across the design space, as in Figure 4-9.

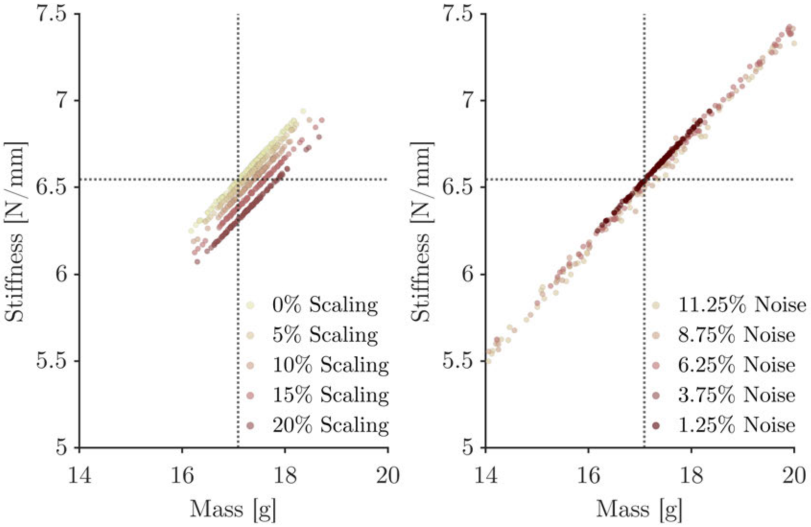

Figure 4-8: Generated lattices for the "Bottom - single" condition at a) fixed noise (1.25%) and b) fixed scaling (0%). The relationships shown in Figures 4-6 and 4-7 apply to individual concentration geometries as well as entire lattice populations. As scaling increases, average stiffness decreases; higher noise levels produce greater range of mass and stiffness.

We can also quantify the ellipse's shape (eccentricity) and position (rotation, or the slope of its major axis), as in Figure 4-10. The eccentricity e of an ellipse is defined as $\sqrt{1 - \frac{b^2}{a^2}}$, where a and b represent the lengths of the semi-major and semi-minor axes, respectively. A circle has $a = b$, and thus zero eccentricity. As an ellipse flattens, its eccentricity increases and approaches 1. A population with a high eccentricity shows less variability in stiffness for a given mass, and the distribution looks much more like a line than a circle. The slope of the major axis is represented in Figure 4-10b as the angle of rotation from the y-axis. This describes how horizontal or vertical the distribution is. Both the eccentricity and rotation angle are relatively constant at noise levels above 5%. Changes in eccentricity and rotation are most noticeable at high scaling and low noise levels. At low noise, there is little variation in mass between lattices, but the high scaling results in significant stiffness differences. This creates a rounder ellipse.

This design space can also be represented by the length of the major and minor axes of the ellipses, as in Figure 4-11. Major and minor axis lengths are relatively decoupled from scaling, as represented by the vertical bands in Figure 4-11a and b. In much of the design space (noise $> 5\%$, scaling $< 10\%$), these mainly change with noise. Comparing the ratio of the minor to major axis lengths, as in Figure 4-11c, shows changes only at combinations of low noise and high scaling levels. For the rest of the design space, the ratio of the axes is similar. This aligns with the ellipses in Figure 4-9b: the ellipses for noise $> 5\%$ and scaling $< 10\%$ have similar shapes but appear uniformly stretched in both directions as noise and scaling changes.

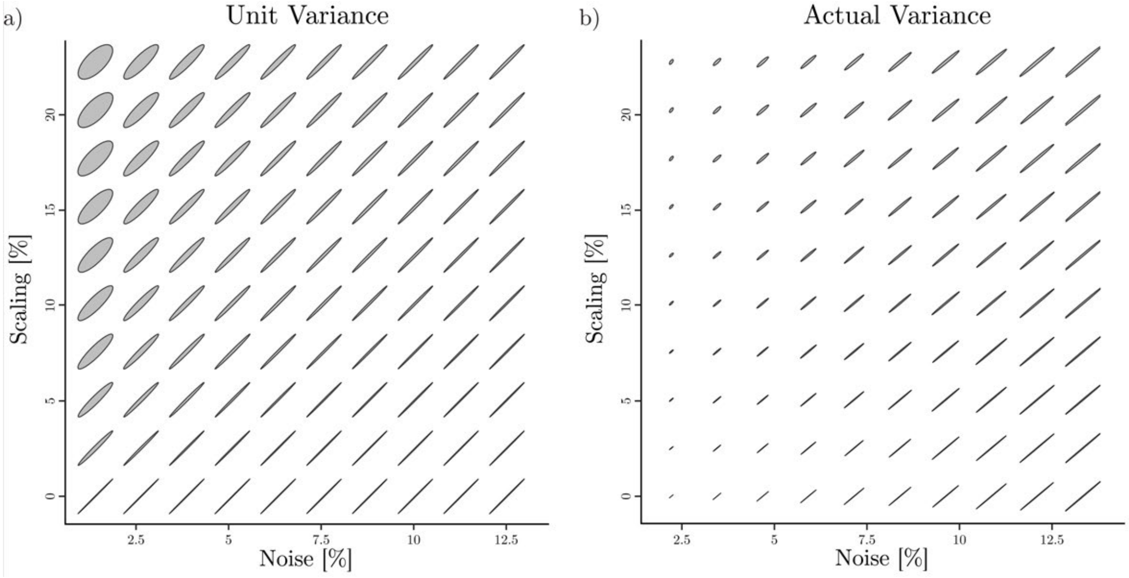

Figure 4-9: Probability distributions characterizing a population of lattices can be represented as ellipses aligned with the first singular vector of the distribution. The shaded region represents a 95% confidence interval. a) Scaling distributions to unit variance in both the mass and stiffness directions shows change in ellipse shape across the design space. b) Plotting distributions with their actual variances demonstrates the ellipses shows change in ellipse size across the design space.

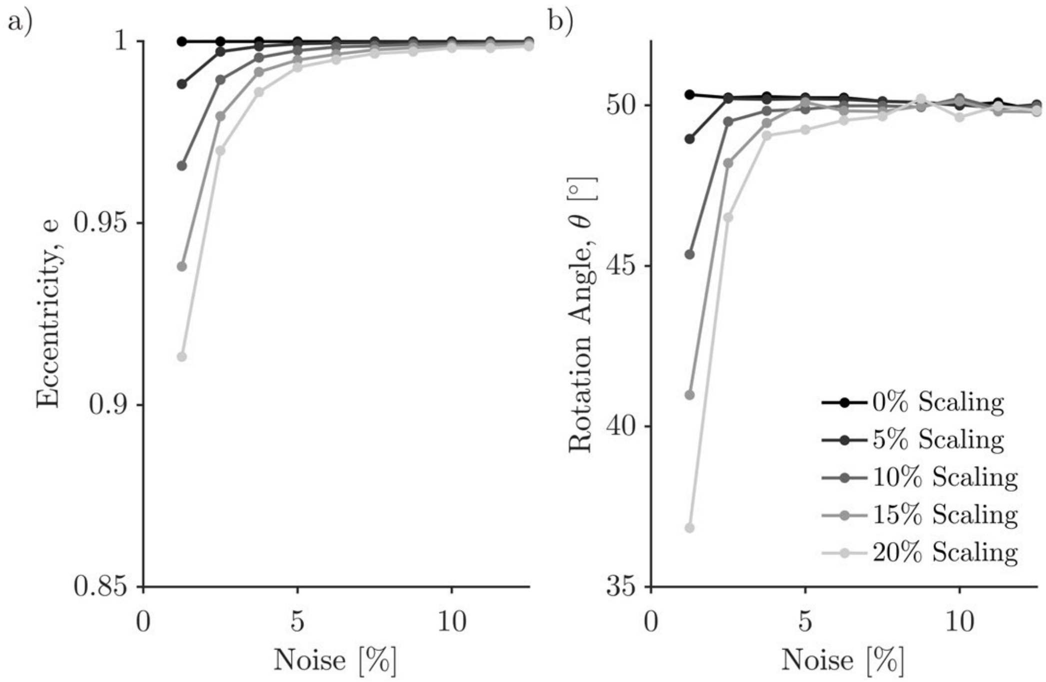

Figure 4-10: Distribution eccentricity (a) and rotation angle (b) are high once noise exceeds above approximately 5%, regardless of scaling. Both eccentricity and rotation angle decrease with increasing scaling, and this effect is most pronounced at low noise levels.

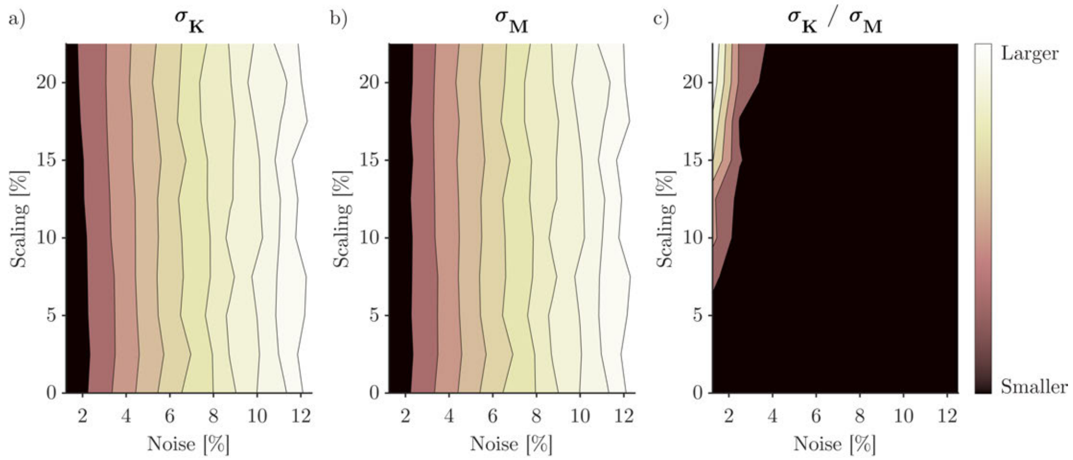

Figure 4-11: Standard deviations of stiffness (a) and mass (b) of characterized lattice populations shown with the ratio of the standard deviations (c). Standard deviations are governed by noise; other than combinations of low noise and high scaling, the ratio of the standard deviations is similar across the design space.

Chapter 5

Framework for Analyzing Test Accuracy

5.1 Statistical Quality Control

As we saw with the mass and stiffness data of Figure 2-15, data from manufacturing processes is often normally distributed about some average value. A machining process producing shafts, for example, will output shafts with diameters following a bell-shaped distribution, as in Figure 5-1a. This distribution centers about the average diameter of $\bar{x}$, given by

$$\bar{x} = \frac{x_1 + x_2 + x_3 + \ldots + x_n}{n}, \tag{5.1}$$

The dispersion, or width of the curve is described using the standard deviation σ_x, where

$$\sigma = \frac{\sqrt{(x_1 - \bar{x})^2 + (x_2 - \bar{x})^2 + \ldots + (x_n + \bar{x})^2))}}{n - 1} \tag{5.2}$$

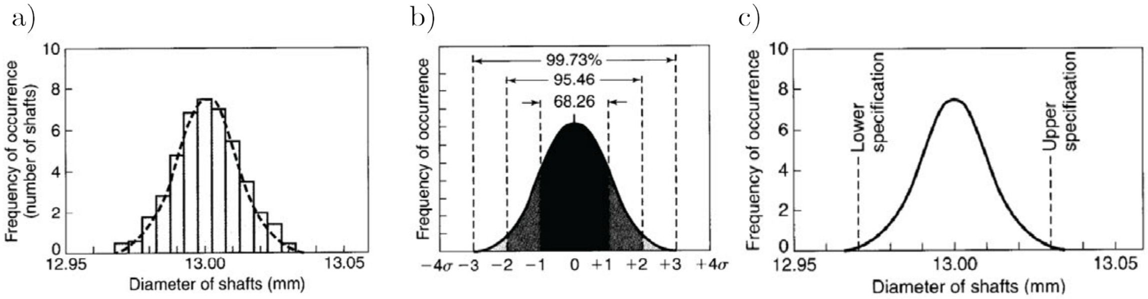

Figure 5-1: a) Histogram of the diameters of measured shafts from a machining process. b) Bell-shaped, normal distribution curve indicating regions within each range of the standard deviation. c) Gaussian frequency distribution showing sample upper and lower specification limits [40].

Together, Equations 5.1 and 5.2 define a probability density function (PDF), $f(x)$, where $f(x)$ represents the probability that random variable f's value would equal x. For the Gaussian distribution, this relationship is written as

$$f(x) = \frac{1}{\sqrt{2\pi}\sigma_x} \exp\left(-\frac{(x-\bar{x})^2}{2\sigma_x}\right), \tag{5.3}$$

Integrating across a range of x values creates a cumulative distribution function (CDF), written as $F_x(x)$, where $F_x(x)$ represents the probability that the random variable takes on a value less than or equal to x. In a manufacturing environment, we might want to compute the probability that a measured dimension falls within an acceptable range. For the normal distribution, 68.26% of the population fall within $\pm 1\sigma$, 95.46% within $\pm 2\sigma$, and 99.73% within $\pm 3\sigma$.

Specification limits govern which parts from a process are accepted. These are often defined based on customer needs or interaction with other components in a device. For a shaft, a specification limit may be governed by the amount of acceptable tolerance in a bearing fit. For a running shoe midsole, specification limits might be set to create pairs of shoes which feel the same to a runner. Specification limits are commonly described in terms of standard deviations from the mean. The relationship between the specification limit and σ dictates the rate of defective parts.

Many companies utilize six sigma principles, which emphasize process capabilities and producing defect-free parts. At a six sigma quality standard, the specification limit falls at $\pm 3\sigma$ of the average, producing 0.27% defective parts, or 2700 defects per million parts produced. As σ increases relative to the specification limit, the defect rate increases. By comparison, a four-sigma level accepts parts within $\pm 2\sigma$, giving a 4.54% defect rate. At smaller standard deviations, this means more parts automatically meet the specification. As a result, the likelihood of correctly guessing a part's viability by chance increases.

5.2 Comparison of Real and Simulated Data

A bivariate normal distribution was fit to the physical mass and 9 mm stiffness data described in Section 2.4. This distribution is described by matrices $\boldsymbol{\mu}$ and $\boldsymbol{\Sigma}$:

$$\boldsymbol{\mu} = \begin{bmatrix} \mu_M & \mu_K \end{bmatrix} = \begin{bmatrix} 21.8 & 66.0 \end{bmatrix} \tag{5.4}$$

$$\boldsymbol{\Sigma} = \begin{bmatrix} \sigma_M^2 & p\sigma_M\sigma_K \\ p\sigma_M\sigma_K & \sigma_K^2 \end{bmatrix} = \begin{bmatrix} 3.7 & 21.9 \\ 21.9 & 147.0 \end{bmatrix} \tag{5.5}$$

The units of the entries in $\boldsymbol{\mu}$ and $\boldsymbol{\Sigma}$ correspond to the units for mass (g) and stiffness (N/mm) in the original data set. These stiffness values represent to the average stiffness during the first 9 mm of compression (force at 9 mm compression (in N) divided by the compression amount (9 mm).

σ_M, σ_K, and p can be found from covariance matrix $\boldsymbol{\Sigma}$ and compared to the means in $\boldsymbol{\mu}$. This gives $\frac{\sigma_M}{\mu_M} = 0.089$ and $\frac{\sigma_K}{\mu_K} = 0.184$, with covariance $p = 0.935$. Although

$\frac{\sigma_K}{\mu_K}$	σ_K for $\mu_K = 450$ N	σ Cutoff at $K_{Lim} =$		
		5%	10%	20%
0.033	15	1.5	3	6
0.067	30	0.75	1.5	3
0.1	45	0.5	1	2

Table 5.1: Specification limits are set as a percentage above/below the mean but can also be expressed in terms of the standard deviation.

the standard deviations are comparable to those generated at various noise levels from the numerical solver, the covariance is lower than most distributions generated by the solver. The generated distributions had covariance values as low as 0.7, but most were between 0.95 and 1.

This difference likely results from the two different cell geometries used in physical testing vs. simulation. The stiffness of rhombic dodecahedron unit cells, which were used in the physical testing, scales with the square of its relative density, ρ_{rel}^2. The stiffness of the octet truss lattice, used in the computational model, scales with the relative density.

$\boldsymbol{\mu}$ and $\boldsymbol{\Sigma}$ can also be found for the bivariate normal PDF centered about (0, 0) and scaled to reflect percentiles above/below the mean, as in Section 4.4.

For the physical rhombic dodecahedron lattices, $\pm 1\sigma_K$ represents stiffnesses $\pm 18.4\%$. In a well-controlled manufacturing process, standard deviations would be small relative to the average stiffness. Although specification limits are set as percentiles relative to the mean, comparing these limits to the standard deviation helps with comparing distributions. Midsole-level physical compression testing yields an average stiffness μ_K of approximately 450N. The relationship between standard deviation is outlined for selected hypothetical values of σ_K and K_{Lim} in Table 5.1. The accuracy of a test method will depends on the specification limit as a function of the standard deviation. For two distributions with the same covariance, accuracy will be the same at the same number of standard deviations above/below the mean: accuracy will be the same at $K_{\text{Lim}} = 10\%$ for a distribution with $\sigma_K = 15$ as it will be at $K_{\text{Lim}} = 20\%$ when $\sigma_K = 30$.

5.3 Test Accuracy as a Function of Specification Limit

The goal of this section is to understand how well mass predicts stiffness for simulated lattices produced with various amounts and types of manufacturing noise. By studying how modifying each type of noise impacts accuracy, we can understand how a test's accuracy would change if certain aspects of the manufacturing became better controlled. Although the test accuracy is visualized as a function of the noise and stiffness used to create the lattice population, the analytical framework applied to each population is easily applied to other sets of mass data and/or data collected from other testing techniques, provided it is normally distributed.

First, a simple go/no go test is developed using a linear regression model. For each population of lattices, the regression model's fit parameters were used to establish upper and lower mass cut off limits based on potential stiffness specifications. Next, the bivariate Gaussian distributions characterized in Section 4.4 are used to see if these mass cut offs can be modified to produce higher accuracy than regression model.

For each population of n samples, $3 \times n$ matrices $\mathbf{W_a}$ and $\mathbf{W_p}$ contain the actual and predicted results, respectively. $\mathbf{W}$'s rows represent whether the specimen is under the lower limit, within the acceptable range, or above the upper limit. Each column $i = 1 : n$ represents the result for lattice i.

$$\mathbf{R} = \frac{1}{n}\mathbf{W_a}\mathbf{W_p^T} \tag{5.6}$$

contains the results for the test. Multiplying $\mathbf{W_a}$'s columns with $\mathbf{W_p}^T$'s rows gives R as a sum of n rank-one matrices, where each rank-one matrix represents the type of result (false/true, positive/negative) for a single lattice. As a result, rows of $\mathbf{R}$ represent the actual results while columns represent the predicted results. Values along $\mathbf{R}$'s diagonal represent correct results: the predicted region matches the actual region.

While unlikely, a test could reject a lattice for the incorrect reasons. A lattice with low mass but abnormally high stiffness (above the upper stiffness specification) could be rejected, as could a very heavy lattice with low stiffness (below the lower stiffness specification). These results are represented by R_{13} and R_{31} and shown by the upper left and lower right regions (in red) in Figure 5-2. Although the test rejects these lattices for incorrect reasons, they should be counted as accurate results. A modified results matrix $\mathbf{R}'$ accommodates this, where

$$\mathbf{R}' = \begin{bmatrix} R_{11} + R_{31} & R_{12} & 0 \\ R_{21} & R_{22} & R_{23} \\ 0 & R_{32} & R_{13} + R_{33} \end{bmatrix} \tag{5.7}$$

In this study, accuracy is computed as the percentage of correct results. This can be defined as the trace of $\mathbf{R}'$, or the sum of the components along its diagonal. The rates of false negatives ($R'_{21} + R'_{23}$) and positives ($R'_{12} + R'_{32}$) are also determined. Depending on the application, the types of incorrect results may have different relative costs. In medical testing for infectious diseases a high false negative rate could allow contagious individuals to go undiagnosed, unknowingly transmitting the virus to others; however, an increased false positive rate might mean patients who test positive might need additional testing to validate initial result. With more information on the relative costs of each type of false results, false positives and negatives could be weighted differently to better represent the value a test provides, as in Section 5.4.

5.3.1 Least Squares Regression Model

A least squares regression model was used to find the slope and intercept for each distribution, as in Section 2.4 and Figure 2-14. The results of the regression model are visualized as a fit line on the stiffness-mass plot, as in Figure 5-3a for a representative simulated distribution and Figure 5-4a for physical lattices. The shaded region

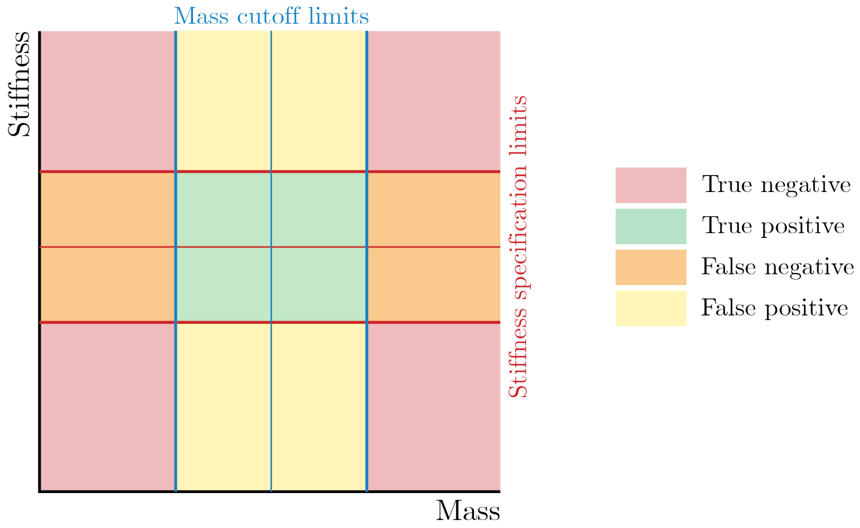

Figure 5-2: Schematic of the types of results produced with given specification limits (red lines) and mass cutoffs (blue lines). Different types of results (true/false and positive/negative) are visualized by shading regions of the graph.

represents 95% confidence based on uncertainty in the fit parameters.

The upper and lower mass cutoff limits are found by solving $y = ax + b$ using the fit parameters (a, b) from the least squares solution and the specification limit, K_{Lim}. As the specification limit decreases, the red lines on Figure 5-3a move inward, and the mass cutoffs (blue lines) adjust accordingly. Least squares finds the "best" mass cutoff by minimizing the vertical distance between data points and the fit line in Figure 5-3a and 5-4a. The regression sets M_{Lim} set based on the regression, and the best fit line approximately aligns with the major axis of the probability distribution, such as those shown in Figure 4-10. This means that results matrix $\mathbf{R}$ is very close to symmetric, and the false negative rate will be very similar to the false positive rate, regardless of the specification limit.

Figure 5-3b displays the accuracy of this test as a function of the specification limit for one distribution, represented by the black line. The false positive and negative rates are included in grey. The red line represents a specification limit of $\pm 5\%$, which corresponds to the red lines drawn in Figure 5-3a. At low and high specification limits, accuracy is very close to 1, but it decreases at intermediate levels. The magnitude and location of this minimum vary with the distribution. For distributions with higher fit uncertainty (represented here as width of the grey shaded band in Figure 5-3a), the worst accuracy is much lower than for distributions with smaller uncertainty intervals.

Accuracy, false negative, and false positive rates were also found using the representative probability distribution instead of the raw data. The bivariate probability distribution function from Section 4.4 is used to create a cumulative distribution function for each group of lattices. Evaluating the cumulative distribution function gives the percentage of samples in each of the nine rectangular regions of Figure 5-2. This creates the 3 by 3 matrix $\mathbf{R}$, which we modify according to Equation 5.7 to give $\mathbf{R}'$

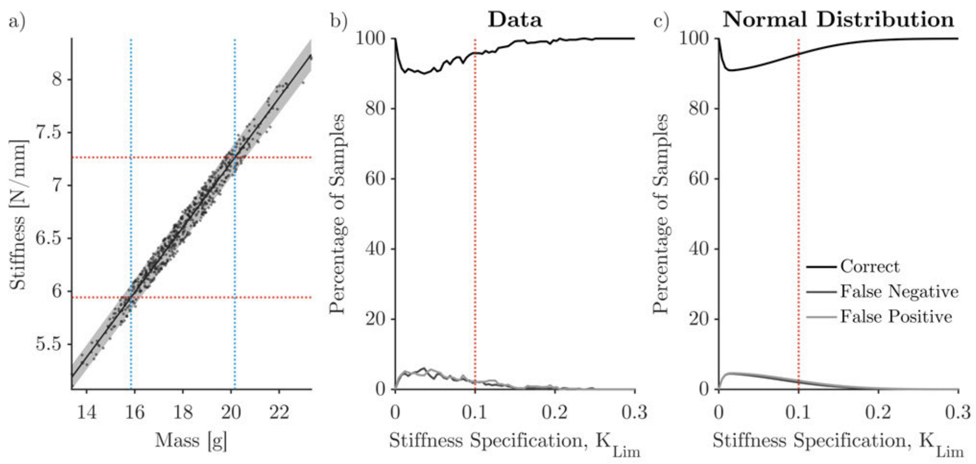

Figure 5-3: Least squares results for simulated octet truss lattices at 5% noise and 10% scaling. a) Lattice data shown by dark grey points, with least squares fit represented by the black line and grey shaded region. Example stiffness specifications (red dotted lines) are set at ±10% of the average stiffness. Mass cutoff limits (blue dotted lines) occur where these lines intersect the best fit line. b) Overall accuracy (black), false positive (light grey) and false negative (dark grey) rates for the lattices generated by the simulation depend on specification limit K_{Lim} but are approximately equal for all limits. c) Smoother results can be obtained by using the bivariate normal distribution for this set of lattices.

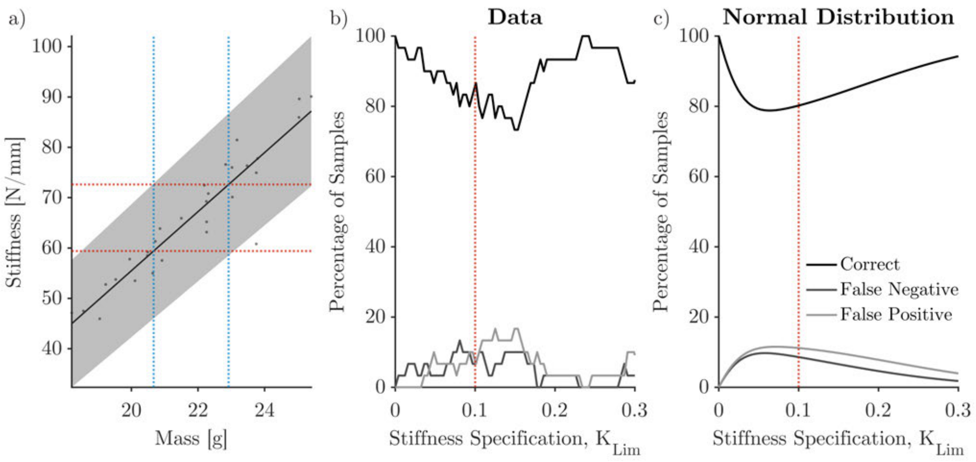

Figure 5-4: Least squares results for physical rhombic dodecahedron lattices. a) Lattice data shown by dark grey points, with least squares fit represented by the black line and grey shaded region. Example stiffness specifications (red dotted lines) are set at ±10% of the average stiffness. Mass cutoff limits (blue dotted lines) occur where these lines intersect the best fit line. b) Overall accuracy (black), false positive (light grey) and false negative (dark grey) rates for the lattices generated by the simulation depend on specification limit K_{Lim} but are approximately equal for all limits. c) Smoother results can be obtained by using the bivariate normal distribution for this set of lattices.

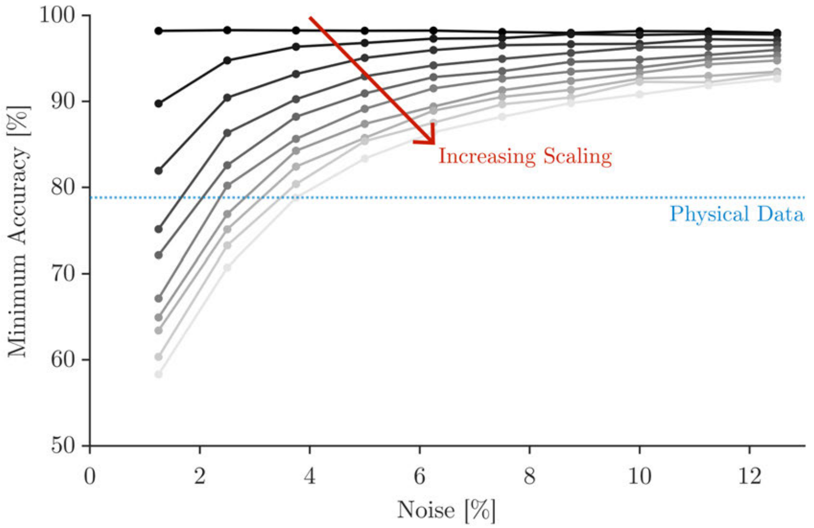

Figure 5-5: Minimum accuracy for the least squares solutions for simulated lattices are shown in grey. Darker lines represent lattices with less scaling. The minimum accuracy for the physical rhombic dodecahedron lattices is represented by the blue dotted line. At low scaling, accuracy is high and changes little with noise. For all scaling levels, accuracy shows little variation once noise $> 7\%$.

and find the overall accuracy at a given mass and stiffness combination. These results are shown in Figures 5-3c and 5-4c. Raw data is discrete and not perfectly normal, which means results are much smoother for both simulated and physical data. For both types of lattices, the raw data shows good alignment with the computation from the normal distribution.

Additional results for a variety of simulated distributions are available in Appendix A.

5.3.2 Modifying Cutoffs Using Bivariate Distributions

Section 5.3.1 uses least squares to find the "best" mass cutoff for a given specification limit. As a function of the mass and stiffness limits, the total accuracy takes the shape of a saddle, as shown in Figure 5-7a.

When the mass limit is too low, false negative results dominate; too few samples are accepted, and good samples are incorrectly rejected. At higher mass limits, false positive results dominate; too many samples are accepted. At high stiffness limits, accuracy is generally high, which makes sense; at high specification limits, most samples should meet the specification, and expected accuracy will increase. Least squares provides a solution along the crest of the accuracy surface, represented by the darker regions of Figure 5-7a.

Taking slices along specific specification limits more clearly reveals the impact of changing the acceptable mass limit, M_{Lim}. The product needs define the specification limit, and we hope to find the mass cutoff which yields the highest accuracy. A slice

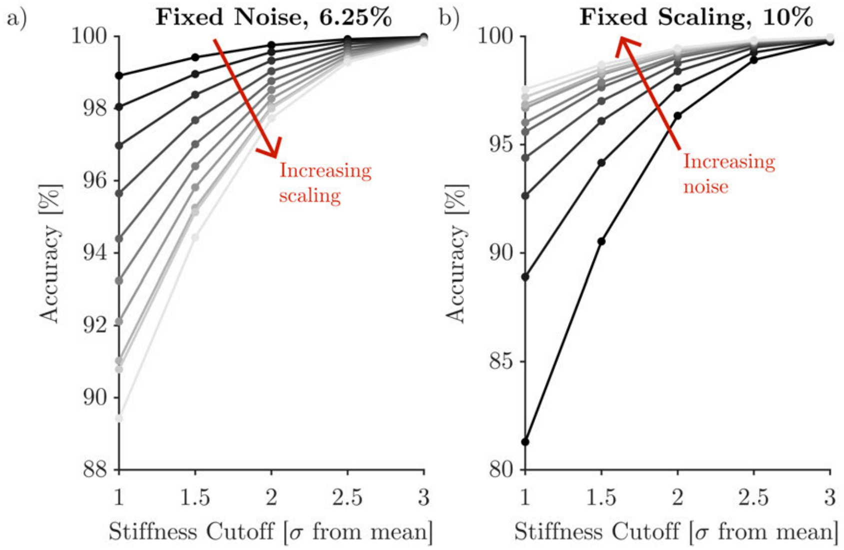

Figure 5-6: Accuracy of least squares solution increases as more samples meet the specification limits, represented by increasing the stiffness specification (x-axis). At constant noise (a), increasing scaling (lighter lines) decreases accuracy. At constant scaling (b), increasing noise (lighter lines) increases accuracy.

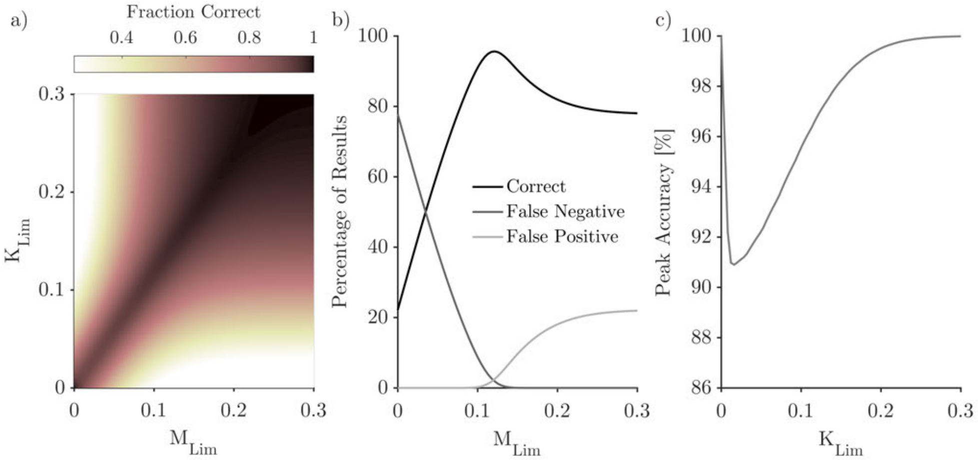

Figure 5-7: a) Heatmap displaying the overall accuracy of mass as a prediction of stiffness. b) A slice through a) at $K_{\text{Lim}} = 0.10$ reveals the mass cutoff limit to maximizes accuracy and shows a breakdown of the false positive (red) and negative (blue) rates. At the maximum accuracy, false positive and negative rates are exactly equal. c) The magnitude of this peak accuracy depends on the specification limit but is overall quite high.

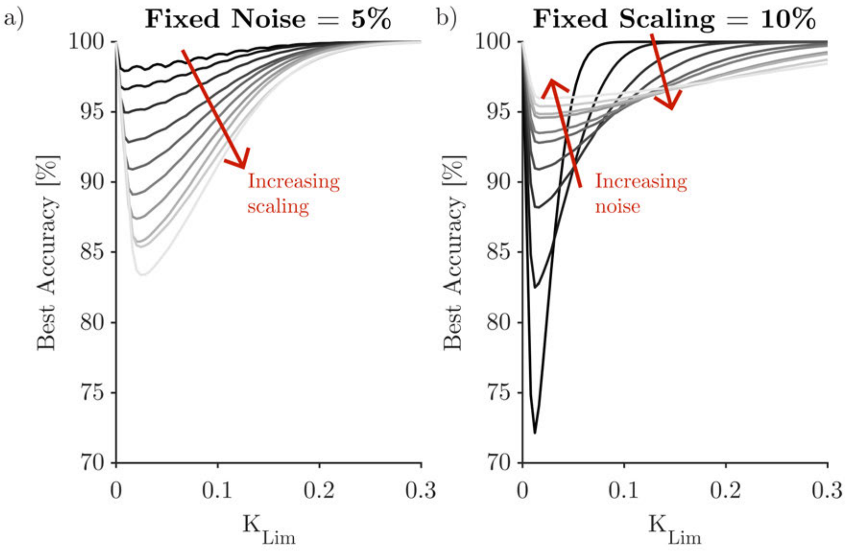

Figure 5-8: Best accuracy from adjusting cutoff limits, shown as a function of stiffness specification. At fixed noise (a), accuracy decreases with increasing scaling (lighter lines). At fixed scaling (b), the best accuracy increases with increasing noise (lighter lines) for low K_{Lim} but decreases with increasing noise for larger K_{Lim}.

along Figure 5-7b at $K_{\text{Lim}} = 0.05$ is shown in Figure 5-7c. At low values of M_{Lim}, incorrect results are dominated by false negatives. The testing limits are too narrow, meaning lattices which meet the specification are falsely rejected. As M_{Lim} increases, false negatives decrease, and false positives increase. Overall accuracy is highest where the false positive rate exactly equals the false negative rate. This magnitude and location of this optimum accuracy depend on both the stiffness specification limit and the underlying distribution of lattices. Appendix A contains graphs similar to those in Figure 5-7 for additional distributions.

Fixing the noise level and creating plots similar to Figure 5-7c shows the impact of scaling, represented in Figure 5-8a. At a low strut noise level (1.25%), increasing scaling causes the best accuracy to decrease. A similar shape (global minimum followed by a plateau) is observed for all distributions. Accuracy is generally high for $K_{\text{Lim}} > 12.5\%$ and varies little as scaling and stiffness specification limit increase.

5.4 Minimizing Cost of a Hybrid Testing Approach

The best accuracy found at each stiffness level by sampling the probability distribution function is the same as that from the least squares regression model. The best accuracy from the bivariate distribution occurs when the false negative and positive rate were exactly equal. Least squares provides a solution where false negative and positive rates match (approximately equal regardless of specification limit). As a result, both techniques have high accuracy at low specification limits which decreases as the specification limit increases.

Although these techniques maximize accuracy by producing equal false positive

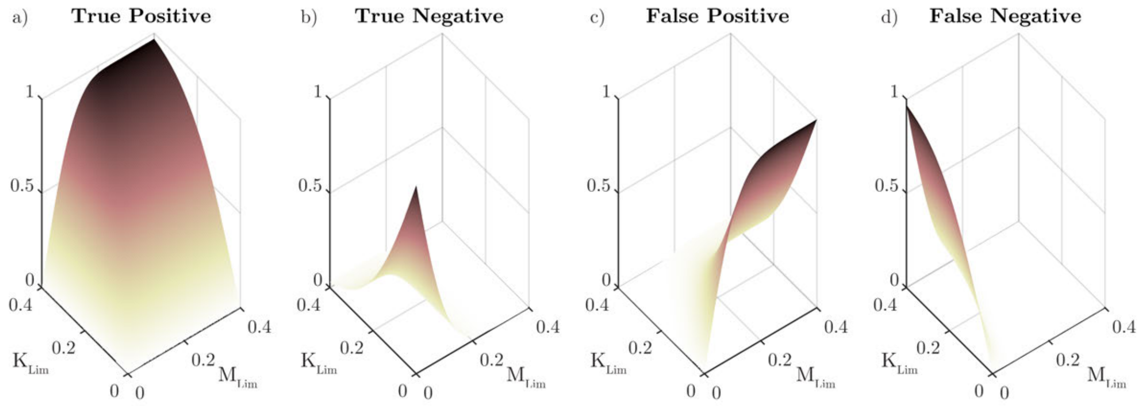

Figure 5-9: The breakdown of types of results from using mass to predict stiffness depends on the mass and stiffness limits. At higher specification (stiffness) limits, more samples are expected to meet the standard.

and negative rates, this may not be the ideal solution. The types of results in $\mathbf{R}'$ from Equation 5.7 depend on the mass and stiffness specifications, as shown in Figure 5-9. Adjusting $\mathbf{R}'$ to apply penalties to different types of results shifts the breakdown of false negative or positive results. In a well-controlled manufacturing environment, most parts should meet the specification. We believe that most of the parts which are accepted *should* be accepted, and a low false positive rate gives high confidence that default parts are accepted. Favoring false negative results might require a secondary test for rejected parts in order to avoid incorrectly rejecting good midsoles.

With information about relative costs for the two tests, different types of optimization problems can be formulated to minimize cost. Without knowing the relative cost of false positive results, we can minimize testing cost C, subject to some minimum accuracy level A:

$$C = c_1(T_N + T_P + F_N + F_P) + c_2(T_N + F_N) \tag{5.8}$$

$$A = T_P + T_N + F_N \tag{5.9}$$

where c_1 and c_2 represent the cost of the initial and secondary tests, respectively, and T_N, T_P, F_N, F_P are the fraction of true negative, true positive, false negative, and false positive results, respectively. In this model, all samples undergo initial test with cost c_1. Rejected samples (all negative results) then proceed to a second test with cost c_2, which has 100% accuracy. Overall accuracy of this hybrid test protocol includes true positive results, which are initially accepted, as well as both types of negative results. Cost C is driven by the rate of negative results, $T_N + F_N$. Testing cost is represented by the shading on Figure 5-10 for $[c_1, c_2] = [1, 10]$. Contour lines represent varying accuracy levels A; as desired accuracy increases, fewer samples are accepted from the initial test.

The minimum cost to achieve each accuracy level in $Figure\ 5 - 10$ is shown in Figure 5-11 as a function of k_{Lim}. For a specification limit of $\pm 1\sigma_k$, represented by

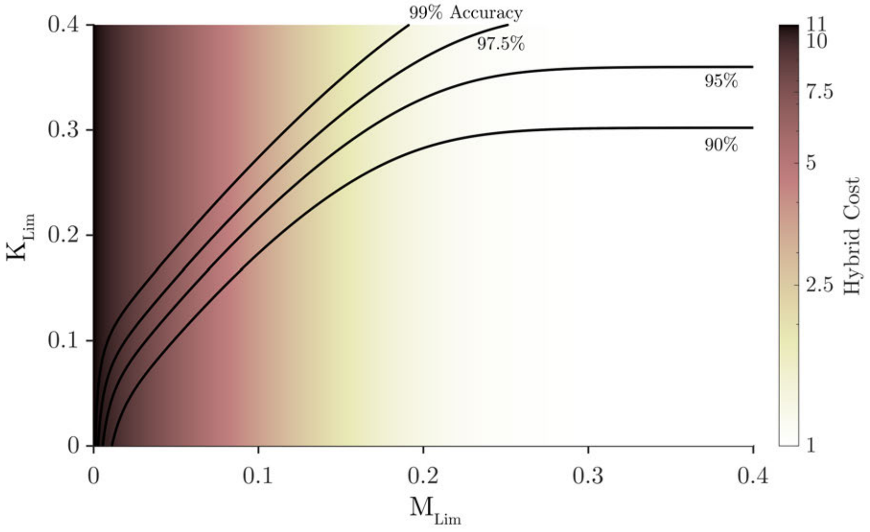

Figure 5-10: Total cost of a hybrid test depends on the mass limit, which dictates the rate of negative results. Cost is independent of the specification limit, represented by shading in this graph. Black contour lines represent accuracy levels of 90, 95, 97.5, and 99%. As cost decreases with M_{Lim}, the minimium cost to achieve a required accuracy occurs exactly along the contour lines. Higher accuracy results in higher cost.

the vertical line, the hybrid test achieves 99% accuracy at 70% of the cost to perform the secondary test on all samples. This relationship holds even as the distribution's standard deviation changes relative to the mean. For this physical data, $\pm 1\sigma_k$ corresponds to a k_{Lim} of 18%. As the process becomes better controlled, $\pm 1\sigma_k$ will match a lower k_{Lim} value, but the cost to achieve that result will not change.

Operating at a two-sigma level (accepting parts ± 1 standard deviation of the mean) is rare in manufacturing, where processes often run at four-sigma or higher. At four-sigma, the cost to achieve 99% accuracy is only 20% that of the secondary test, showing significant cost savings while maintaining high accuracy.

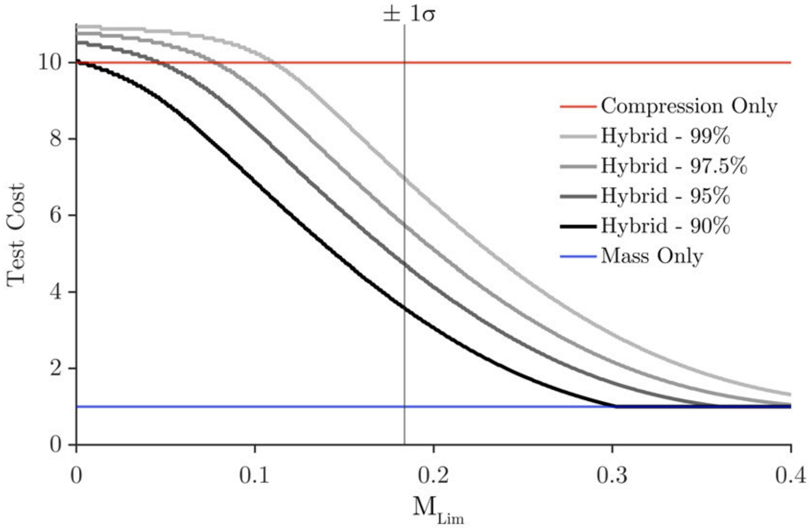

Figure 5-11: Cost of the hybrid test depends on both the specification limit and the desired accuracy level. At small specification limits, it is more expensive to use the hybrid test than to test all samples with a compression test. Achieving high overall accuracy means reducing the false positive rate, meaning most samples are rejected. Cost decreases with decreasing accuracy and increasing specification limit. At $\pm 1\sigma$, the hybrid test achieves 99% accuracy at 69.8% of the cost for the current test. At $\pm 2\sigma$, achieving 99% accuracy requires only 16.4% of the current cost.

Chapter 6

Conclusions and Next Steps

This study presents data on the mechanical and acoustic properties of additively manufactured lattices and outlines a framework for evaluating the accuracy of test methods. It also describes a two-test hybrid protocol which achieves high accuracy at a significant cost reduction compared to existing testing.

Standard compression testing established the stiffness of flexible AM lattices, and mass, volume, and acoustic tests were pursued as alternate ways to estimate lattice stiffness. Stiffness data revealed that differences in lattice geometry are responsible for a proportion of variance omega-squared over five times that resulting from material differences (0.716 vs 0.129). Geometric changes appear as variations in strut thickness, and material changes might manifest as local or global differences to the bulk solid's properties (density, elastic modulus). Overall material density was constant for lattices printed under both light intensity levels and matched the manufacturer's advertised density. With a constant material density, geometric changes can be determined either through mass or volume.

Both mass and volume measurements showed strong correlations with lattice stiffness and good repeatability. Due to the lower uncertainty between individual mass measurements (0.030%) compared to volume measurements (9.2%), analysis focused on using mass as a predictive tool. Ultrasonic pulse-echo testing was also explored as a potential test method and also shows statistically significant correlations ($p = 0.0398 < 0.05$). Additional data is still needed to increase confidence in this test method, but the test is a promising and unique alternative to compression testing.

A numerical solver was also used to simulate compression testing of lattices with manufacturing variability. Mass and stiffness of both the physical and simulated lattices followed a bivariate normal distribution. The accuracy of mass as a predictive tool was established for simulated lattices with different amounts and types noise as well as the physical lattices. Based on the range of stiffnesses to accept, the range of acceptable masses can be set using a simple least-squares regression model. This technique has a minimum accuracy of 78.8% for the physical lattices; at $\pm 1\sigma$, accuracy is 86.3$.

When the least-squares model sets the acceptable masses, the false positive and false negative rates are equal, which may not be favorable as a manufacturing quality test. Reducing the range of accepted masses increases the false negative rate but sharply decreases the false positive rate. As predicting lattice stiffness by measuring mass is quick, repeatable, and low-cost, it could be advantageous to measure mass of all samples, ensure a low false positive rate but produce more false negatives, and then conduct secondary (compression) testing of rejected lattices.

The hybrid testing model determines the minimum cost to measure all samples using the first (inexpensive, mass) test and perform a second, more expensive test (quasi-static compression) on all rejected samples. Achieving 99% accuracy with this protocol lowers cost by 30.1% at a two-sigma specification limit ($\pm 1\sigma$) and by 83.6% at a four-sigma level ($\pm 2\sigma$). With additional understanding of the relative costs (both time and money) required to perform tests, as well as the cost of each type of result, specification limits can be further optimized to minimize cost and maximizing yield. Including a penalty factor to represent the value for users of midsoles with stiffnesses close to the mean could allow for optimization of both specification (stiffness) and testing (mass) limits to minimize cost, which becomes a function of time, money, and value to athletes.

The hybrid test results are promising, and the accuracy framework is parameterized from a normal distribution, providing easy application to new sets of physical or simulated data. With a larger sample size of ultrasonic data, this framework could be applied to better understand that method's viability. In addition to collecting ultrasound data for more samples, potential work could explore multiple scattering simulations or other techniques for measuring the acoustic properties of materials with periodic voids or variations in acoustic impedance. Introducing variations to elastic modulus or density of struts in the simulation could be an interesting way to understand the impact of localized material changes on overall effective stiffness.

As an applied test for a manufacturing environment, the same mass-stiffness relationship must be found in midsole-level testing, and the results must be normally distributed in both dimensions. Collecting this data will be a critical step for applying this research in future work. At the end of the day, midsole-level results are what provide true value, but physical and simulated data from this work make a compelling case for using mass as a stiffness prediction tool, even if additional testing is needed for some lattices to optimize cost and manufacturing yield.

Appendix A

Further Results

A.1 Lattice Simulation Results

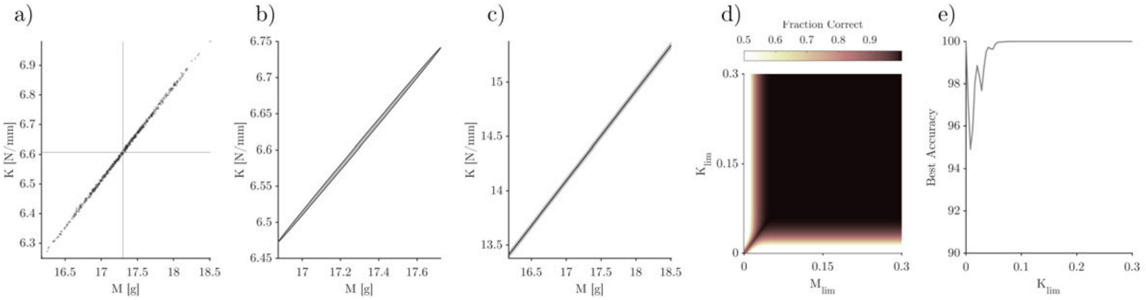

Figure A-1: Results for simulated lattice samples with 1.25% noise and 0% scaling. a) Mass and stiffness of simulated lattices. b) 95% confidence ellipse for normal distribution fit to data. c) Best fit line and uncertainty determined through least squares model. d) Accuracy obtained by modifying mass and stiffness cutoff limits. e) Peak accuracy as a function of stiffness specification limit. Peak accuracy from modifying mass cutoff matches accuracy of the least squares model.

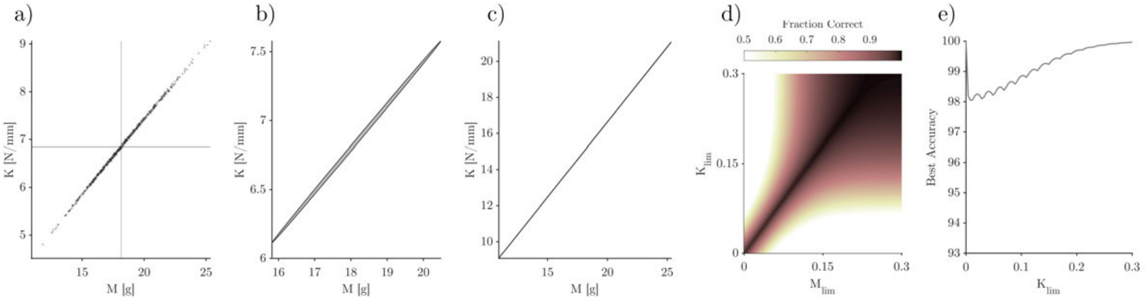

Figure A-2: Results for simulated lattice samples with 6.25% noise and 0% scaling.

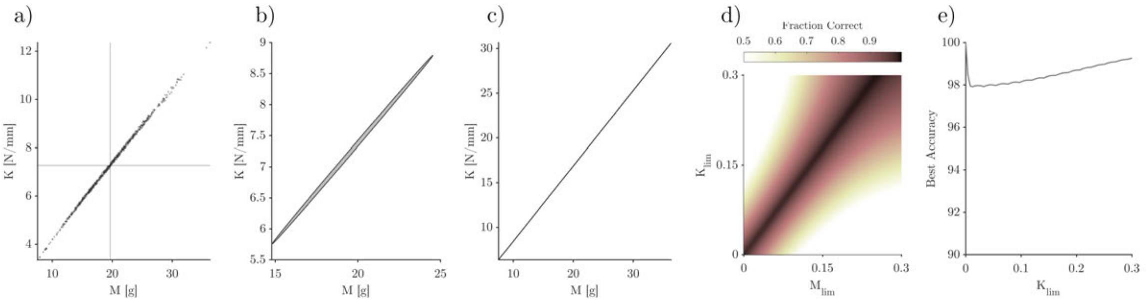

Figure A-3: Results for simulated lattice samples with 12.5% noise and 0% scaling.

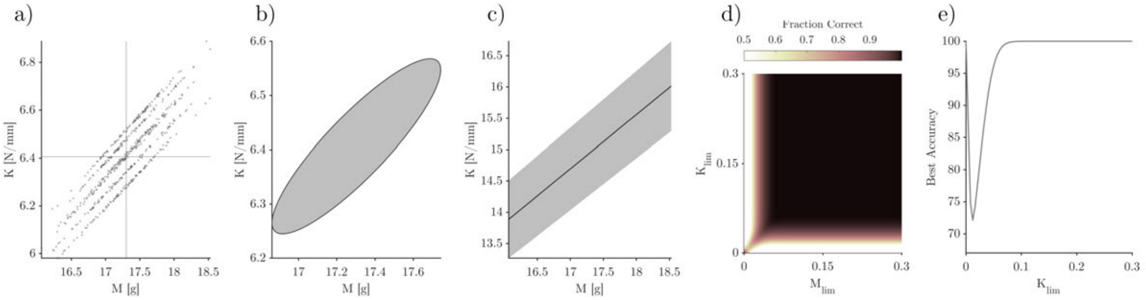

Figure A-4: Results for simulated lattice samples with 1.25% noise and 10% scaling.

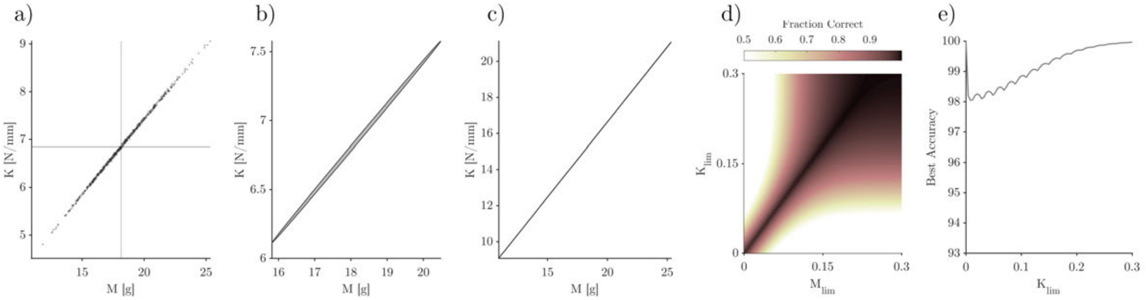

Figure A-5: Results for simulated lattice samples with 6.25% noise and 10% scaling.

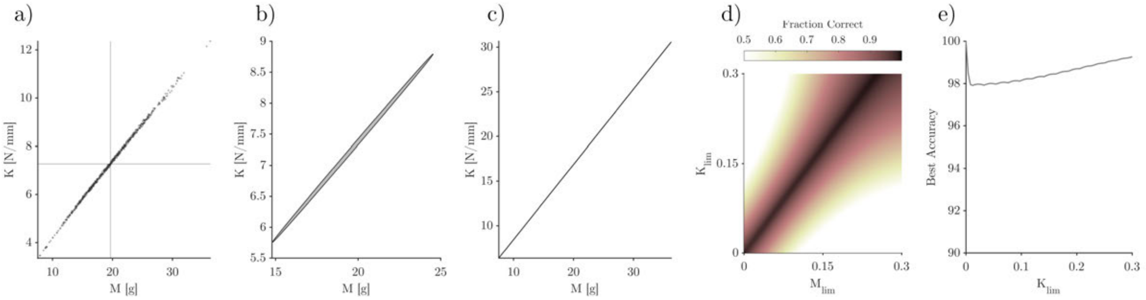

Figure A-6: Results for simulated lattice samples with 12.5% noise and 10% scaling.

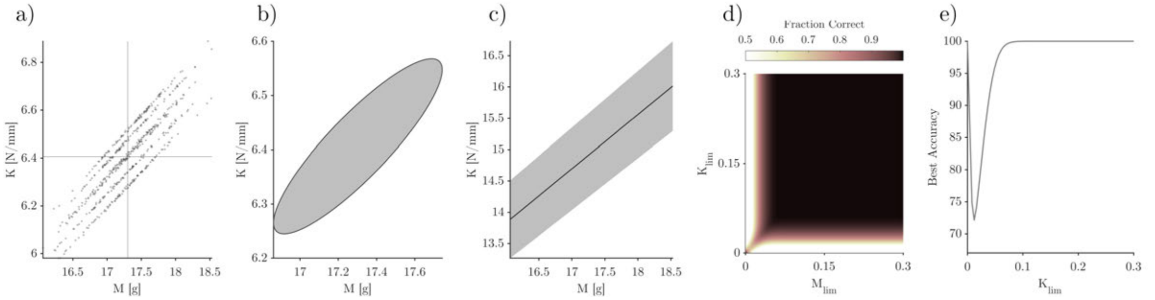

Figure A-7: Results for simulated lattice samples with 1.25% noise and 20% scaling.

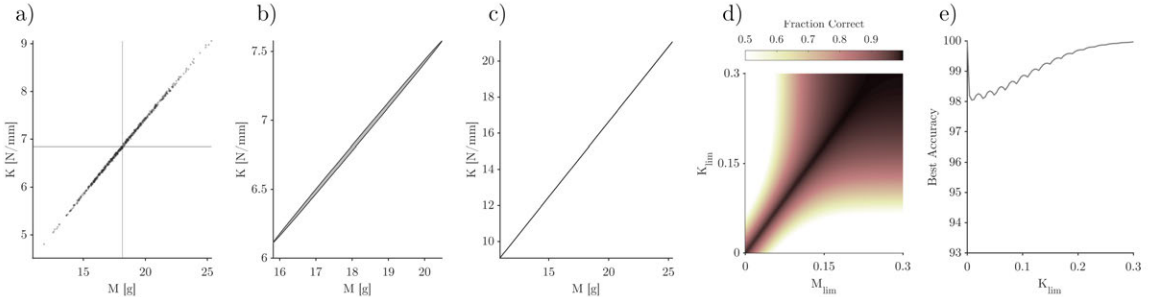

Figure A-8: Results for simulated lattice samples with 6.25% noise and 20% scaling.

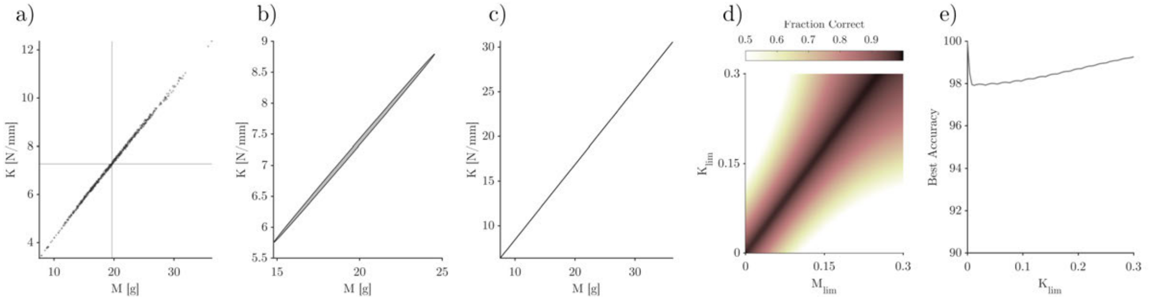

Figure A-9: Results for simulated lattice samples with 12.5% noise and 20% scaling.

Bibliography

[1] Product User's Manual-HCSR04 Ultrasonic Sensor. Technical report, Cytron Technologies, Johor, Malaysia, 2013.

[2] adidas. What is Boost? *adidas*, 2 2020.

[3] adidas AG. adidas 4D Range Expands with New Reflective ALPHAEDGE 4D Running Shoe. Technical report, adidas AG, Herzogenaurach, Germany, 2019.

[4] adidas AG. Ultraboost 19 Shoe, 2019.

[5] M F Ashby. The Mechanical Properties of Cellular Solids. *Metallurgical Transactions A*, 14A:1755–1769, 1983.

[6] Haim Azhari. *Basics of biomedical ultrasound for engineers*. Wiley, 2010.

[7] Sahab Babaee, Babak Haghpanah Jahromi, Amin Ajdari, Hamid Nayeb-Hashemi, and Ashkan Vaziri. Mechanical properties of open-cell rhombic dodecahedron cellular structures. *Acta Materialia*, 60(6-7):2873–2885, 4 2012.

[8] Jennifer Beem and Sarah Fay. Lattice study for midsole design. Technical report, Massachusetts Institute of Technology, Cambridge, 2017.

[9] Jennifer Beem, Sarah Fay, and Paul Lilin. Mechanical Behavior of Lattice Structures. Technical report, Massachusetts Institute of Technology, Cambridge, 2018.

[10] Bruker Nano Surfaces. How Can 3D Optical Profiling Optimize Additive Manufacturing Processes?, 2019.

[11] Carbon 3D. CarbonResin EPU40. Technical report, Carbon 3D, Redwood City, 2018.

[12] Carbon 3D. Dentsply Sirona Lucitone Materials, 2020.

[13] Carbon 3D. How Specialized Transformed the Bike Saddle, 2020.

[14] Carbon 3D. #ProtectItAll, 2020.

[15] Kevin Carlson, Cyanna Moody, Zach Johnson, Ana Flooks, Joshua Graves, and Libby Rickeman. Team Adidas Final Engineering Report. Technical report, Massachusetts Institute of Technology, Cambridge, 2019.

[16] Peter R. Cavanagh. *The Running Shoe Book*. Anderson World, 1980.

[17] Jason Tak Man Cheung, Jia Yu, Duo Wai Chi Wong, and Ming Zhang. Current methods in computer-aided engineering for footwear design. *Footwear Science*, 1(1):31–46, 2009.

[18] Luca Daniel. Lecture 13: Nonlinear steady state analysis a case study, 2018.

[19] V S Deshpande, M F Ashby, and N A Fleck. Foam Topology Bending Versus Stretching Dominated Architectures. *Acta mater*, 49:1035–1040, 2001.

[20] V S Deshpande, N A Fleck, and M F Ashby. Effective properties of the octet-truss lattice material. *Journal of the Mechanics and Physics of Solids*, 49:1747–1769, 2001.

[21] Eastbay. adidas Alphaedge 4D - Men's, 2019.

[22] ElecFreaks. Ultrasonic Ranging Module HC-SR04.

[23] Isabel Flower. Is Mass Customization the Future of Footwear?, 10 2017.

[24] Lee Fok, Muralidhar Ambati, and Xiang Zhang. Acoustic metamaterials. *MRS Bulletin*, 33(10):931–934, 2008.

[25] Formlabs. Stereolithography 3D Printing: From the 1980s to Now. Technical report, Formlabs, Somerville, MA, 2018.

[26] Amanda Furrer. The 5-Minute Guide to Becoming a Running Shoe Expert. Technical report, Runner's World, 2019.

[27] Lorna J. Gibson. Biomechanics of cellular solids. *Journal of Biomechanics*, 38(3):377–399, 2005.

[28] Lorna J. Gibson and M. F. Ashby. *Cellular solids: structure and properties*. Cambridge University Press, New York, 1997.

[29] Young Ki Ha, J. E. Kim, H. Y. Park, and In Won Lee. Propagation of water waves through finite periodic arrays of vertical cylinders. *Applied Physics Letters*, 81(7):1341–1343, 8 2002.

[30] Iain Hannah. *Improving the validity of shod human footstrike modelling with dynamic loading conditions determined from biomechanical motion capture trials*. PhD thesis, Loughborough University, 2014.

[31] Iain Hannah, Andy Harland, Dan Price, Heiko Schlarb, and Tim Lucas. Evaluation of a kinematically-driven finite element footstrike model. *Journal of Applied Biomechanics*, 32(3):301–305, 6 2016.

[32] Jan Hill, Timothy David Lucas, Gerd Rainer Manz, and Paul Leonard Michael Smith. Sole and shoe, 2009.

[33] Wouter Hoogkamer, Shalaya Kipp, Jesse H. Frank, Emily M. Farina, Geng Luo, and Rodger Kram. A Comparison of the Energetic Cost of Running in Marathon Racing Shoes. *Sports Medicine*, 48(4):1009–1019, 4 2018.

[34] Anette Hosoi, Christopher Polster, and Christina Chase. Lattice Stiffness Estimation. Technical report, Massachusetts Institute of Technology, Cambridge, MA, 2019.

[35] Xinhua Hu and C. T. Chan. Refraction of water waves by periodic cylinder arrays. *Physical Review Letters*, 95(15), 10 2005.

[36] Charles W. Hull. Apparatus for production of three-dimensional objects by stereolithography, 1986.

[37] Adam Jane. Material Matters: EVA Foam, 2016.

[38] Rima Janusziewicz, John R Tumbleston, Adam L Quintanilla, Sue J Mecham, and Joseph M Desimone. Layerless fabrication with continuous liquid interface production. *PNAS*, 113(42):11703–11708, 2016.

[39] David Jones. Ariadne. *New Scientist*, page 80, 10 1974.

[40] Serope Kalpakjian and Steven R. Schmid. *Manufacturing Engineering and Technology*. Prentice Hall, Singapore, 6 edition, 2009.

[41] Kishan C Khemani. Polymeric Foams: An Overview. Technical report, American Chemical Society, 1997.

[42] Josef Krautkrämer and Herbert Krautkrämer. *Ultrasonic Testing of Materials*. Springer Berlin Heidelberg, 1990.

[43] C. M. Linton and D. V. Evans. The interaction of waves with arrays of vertical circular cylinders. *Journal of Fluid Mechanics*, 215:549–569, 1990.

[44] O. Lombard, C. Barrière, and V. Leroy. Nonlinear multiple scattering of acoustic waves by a layer of bubbles. *EPL*, 112(2), 10 2015.

[45] Simon Lüdemann. Footwear Report 2019: Athletic Footwear Consumer Market Outlook. Technical report, Statista, 2019.

[46] William E. Masters. Computer automated manufacturing process and system, 1987.

[47] Anne Mündermann, Benno M. Nigg, R. Neil Humble, and Darren J. Stefanyshyn. Foot orthotics affect lower extremity kinematics and kinetics during running. *Clinical Biomechanics*, 18(3):254–262, 2003.

[48] B. M. Nigg, D. Stefanyshyn, G. Cole, P. Stergiou, and J. Miller. The effect of material characteristics of shoe soles on muscle activation and energy aspects during running. *Journal of Biomechanics*, 36(4):569–575, 4 2003.

[49] Benno M. Nigg, Pro Stergiou, Gerald Cole, Darren Stefanyshyn, Anne Mündermann, and Neil Humble. Effect of shoe inserts on kinematics, center of pressure, and leg joint moments during running. *Medicine and Science in Sports and Exercise*, 35(2):314–319, 2 2003.

[50] B.M. Nigg and B. Segesser. Biomechanical and orthopedic concepts in sports shoe construction. *Medicine and Science in Sports and Exercise*, 24(5):595–602, 1992.

[51] Nike. Sneaker science: perfecting the anti-injury shoe, 1 2019.

[52] Nike. Nike Vaporfly 4% Flyknit, 2020.

[53] Stacey O'Connor. Nike Air Max 2017 Fully Reviewed and Compared, 2017.

[54] Keonyoung Oh and Sukyung Park. The bending stiffness of shoes is beneficial to running energetics if it does not disturb the natural MTP joint flexion. *Journal of Biomechanics*, 53:127–135, 2 2017.

[55] PEBAX Powered. A new PEBAX powered shoe to beat your best, 2018.

[56] Jean Pierre R. Roy and Darren J. Stefanyshyn. Shoe midsole longitudinal bending stiffness and running economy, joint energy, and EMG. *Medicine and Science in Sports and Exercise*, 38(3):562–569, 3 2006.

[57] E. Ruffino and P. P. Delsanto. Scattering of ultrasonic waves by void inclusions. *The Journal of the Acoustical Society of America*, 108(4):1941–1945, 10 2000.

[58] Saucony. Saucony Ladies Phoenix 7 Running Shoes 10219, 2015.

[59] Jonathan Sawyer. adidas Springblade "Blue/Silver". *Complex*, 10 2013.

[60] Alex Skvortsov, Ian Macgillivray, Gyani Shankar Sharma, and Nicole Kessissoglou. Sound scattering by a lattice of resonant inclusions in a soft medium. *Physical Review E*, 99(6), 6 2019.

[61] Sneaker News. adidas Is Releasing A 4D-Printed Futurecraft Shoe. *Sneaker News*, 4 2017.

[62] Adrienne So. New Balance's Latest Shoes Come With 3D-Printed Soles. *Wired*, 6 2019.

[63] John F. Swigart. Footwear Sole Component with a Single Sealed Chamber, 2003.

[64] Trefis Team. Adidas Is Giving Nike A Run For Its Money, 2019.

[65] John R. Tumbleston, David Shirvanyants, Nikita Emoshkin, Rima Janusziewicz, Ashley R. Johnson, David Kelly, Kai Chen, Robert Pinschmidt, Jason P. Rolland, Alexander Ermoshkin, Edward T. Samulski, and Joseph T. DeSimone. Continuous liquid interface production of 3D objects. *Science*, 347(6228):1349–1352, 3 2015.

[66] Ronald D. White. Those Nikes — buy, sell or hold? Sneakers are now assets trading like stocks, 4 2019.

[67] Jay Worobets, John William Wannop, Elias Tomaras, and Darren Stefanyshyn. Softer and more resilient running shoe cushioning properties enhance running economy. *Footwear Science*, 6(3):147–153, 6 2014.

[68] Tobias Wunsch, Nathalie Alexander, Josef Kröll, Thomas Stöggl, and Hermann Schwameder. Effects of a leaf spring structured midsole on joint mechanics and lower limb muscle forces in running. *PLoS ONE*, 12(2), 2 2017.